공학석사학위논문

관수로의 전단력을 이용한 미세기포 발생장치에서 나선형 관수로의 설계인자가 기포크기에 미치는 영향

Effect of Helical Pipe's Design Factors on Bubble Size of Splitting-type Fine Bubble Generator

2016년 2월

서울대학교 대학원

건설환경공학부

김 상 범

Abstract

Effect of Helical Pipe's Design Factors on Bubble Size of Splitting-type Fine Bubble Generator

Sangbeom Kim
Department of Civil and Environmental Engineering
The Graduate School
Seoul National University

One of the basic principles of generating fine bubbles (micro/nano bubbles) is splitting the bubbles into smaller bubbles by the wall shear force of a long and straight pipe, which is called a splitter. The aim of this study is to analyze the effect of changing a straight pipe into a helical pipe in a splitting-type bubble generator. The effects of changing each design factor on bubble generation were analyzed using shear force modeling by computational fluid dynamics (CFD), dissolved oxygen (DO) concentration experiment, and bubble size image analysis with confocal microscopy for 10 different designs of splitters.

The results indicated that, with the introduction of a helical radius, the shear force exerted on pipe flow increased, the measured DO concentration increased, and the bubble size decreased. These findings indicate that a helical pipe offers distinct advantages over a straight pipe. Therefore, the introduction of a helical pipe as a splitter would be beneficial in increasing the efficiency of a splitting-type bubble generator.

Keywords: helical pipe, fine bubble, micro/nano bubble, shear force, dissolved oxygen, splitter
Student number: 2014-20552

Table of Contents

List of Tables

List of Figures

Chapter 1. Introduction

1.1 Background

Fine bubbles (or micro/nano bubbles) are widely used in environmental engineering fields. Macro bubbles with a diameter of 300-1,000 ㎛ are used in an aeration process to increase the content of dissolved oxygen in wastewater treatment plants (Motarjemi and Jameson, 1978). Micro bubbles with a diameter of 30-50 ㎛ are used in a flotation process to remove particulate contaminants by attaching to bubbles in a water treatment plant (Edzwald, 1995). Nano bubbles with a diameter of a few nanometer can dramatically increase mass transfer in an advanced oxidation process and a chlorine disinfection process (Agarwal, Ng, & Liu, 2011). Moreover, fine bubbles have the potential to be used in other engineering fields such as semiconductor cleaning, medical and pharmaceutical products, and food processing.

Fine bubbles have a higher mass transfer when the diameter of the bubble gets smaller (Kim, 2010). The larger surface area and slower rising velocity of smaller bubbles makes them stay longer and allows more time for the gas present in the bubble to transfer into water (Kim, 2014). Therefore, generating smaller bubbles is very important.

One of the basic principles of generating fine bubbles is splitting the bubbles into smaller bubbles by the wall shear force of a long and straight pipe, which is called a splitter. The

generator consists of two parts: splitter and pump. Water and air are inserted into a pipe through the pump. While the air-mixed water passes through the pipe, the shear force that the pipe exerts on the passing bubble splits the bubbles into smaller bubbles. An image analysis of the bubbles by using an optical microscope revealed that the average diameter of the bubbles generated by the splitting-type generator was a few hundred nanometer (Kim, 2014).

However, the study on the splitting-type bubble generator only dealt with a straight-pipe splitter. The effect of the shape of the splitter was not considered. According to an earlier study, in a helical pipe, the wall shear stress exerted by the pipe on water increases because of the introduction of torsion by a helical radius (Gammack and Hydon, 2001). Therefore, the use of a helical-pipe splitter instead of a straight-pipe splitter will increase the shear force and generate smaller bubbles.

Moreover, the use of helical pipes will reduce the volume and mass of the splitter, which will increase the mobility and industrial applicability of the generator.

1.2 Objectives

The objectives of this study are to understand the effect of design factors of a helical-pipe splitter on bubble size, and to minimize the volume and mass of the splitter of a bubble generator for extensive industrial applications to industries. The specific objectives are described below:

① To compare the size of bubbles generated by straight-pipe splitters and helical-pipe splitters.

② To analyze the effect of design factors of a helical-pipe splitter on bubble size.

③ To compare the volumes and masses of bubbles generated by hose-coiled helical-pipe splitters and 3D-printed helical-pipe splitters.

1.3 Scope

In this study, fine bubbles refer to artificially manufactured bubbles with a diameter of 100 ㎛ or less based on the scope of ISO/TC 281 Fine Bubble Technology (2013), and the shape of the bubbles is assumed to be a perfect sphere.

Splitting-type bubble generator means a one that uses shear force of pipe flow to split bubbles into smaller bubbles. This bubble generator consists of two parts: a splitter and a pump.

The design factors of a helical-pipe splitter are limited to length, diameter, roughness, helical radius, and pitch. Tapering section and the inner structure of the pipes are not considered in this study.

Chapter 2. Literature Review

2.1 Conventional bubble generators

2.1.1 Pressure drop type: Bubble generator in dissolved air flotation (DAF)

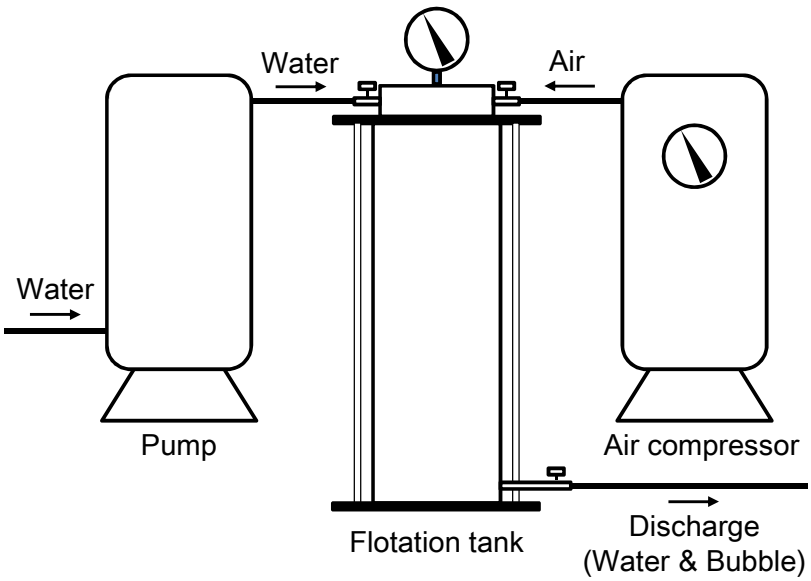

Fig. 2.1 Schematic diagram of
bubble generator in dissolved air flotation (DAF)

Pressure drop type bubble generators are widely used in dissolved air flotation (DAF), which is a water-treatment process that is commonly used for industrial wastewater treatment, natural gas processing, and general water treatment, etc. (Wang, Hung, Lo and Yapijakis, 2004; Kiuru and Vahala, 2001). Fig. 2.1 shows the schematic diagram of the pressure drop type bubble generator.

The generator dissolves air in the water under pressure at 5-6 atm using an air compressor, and then releases the air at atmospheric pressure in a flotation tank. The bubble formation occurs at nucleation sites on the surface of the suspended particles (Scardina, 2000). Generally, the bubble size generated from this device is known to be about 30-50 ㎛ (Dockko and Han).

2.1.2 Enhancement of pressure drop type using orifices: Bubble generator in super-speed impeller flotation (SIF)

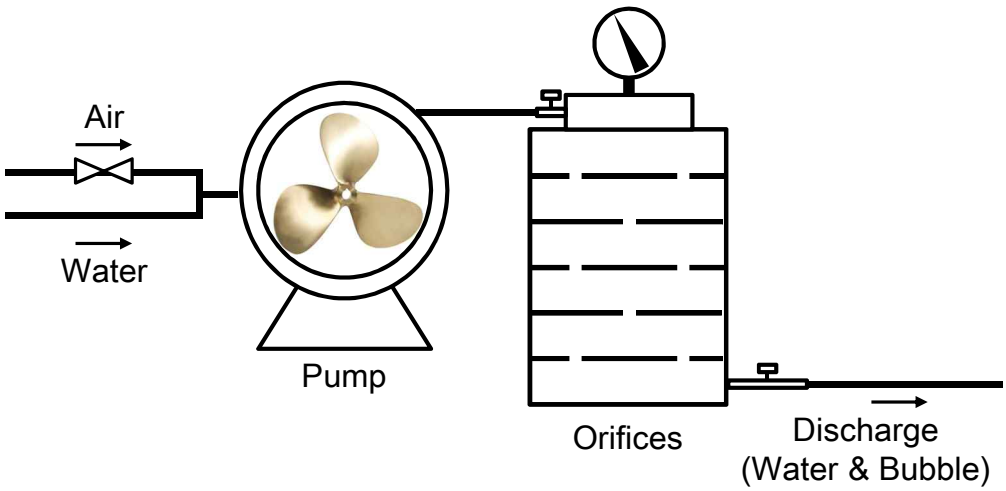

Fig. 2.2 Schematic diagram of
bubble generator in super-speed impeller flotation (SIF)

To conserve energy and reduce the operational cost of the conventional DAF process, Kim (2010) developed a super-speed impeller flotation device (SIF) that used orifices in the mixing chamber of a pressure drop type bubble generator. The generator consists of a pump, mixing chamber with orifices, and a nozzle. Fig. 2.2 describes the schematic diagram of the bubble

generator used in the SIF. It is known that the introduction of orifices may limit the size of generated bubbles to 5-30 ㎛ (Kim, 2010). One noticeable difference is that this generator operates using commercially available pumps, and does not require an air compressor.

2.1.3 Splitting-type bubble generator

In order to reduce the bubble size down to the sub-micron scale, Kim (2014) developed a splitting-type bubble generator that uses shear force to split bubbles into smaller ones. The generator consists of a regular pump and a thin and long pipe, which is called a splitter. Fig 2.3 describes the schematic diagram of the splitting-type bubble generator.

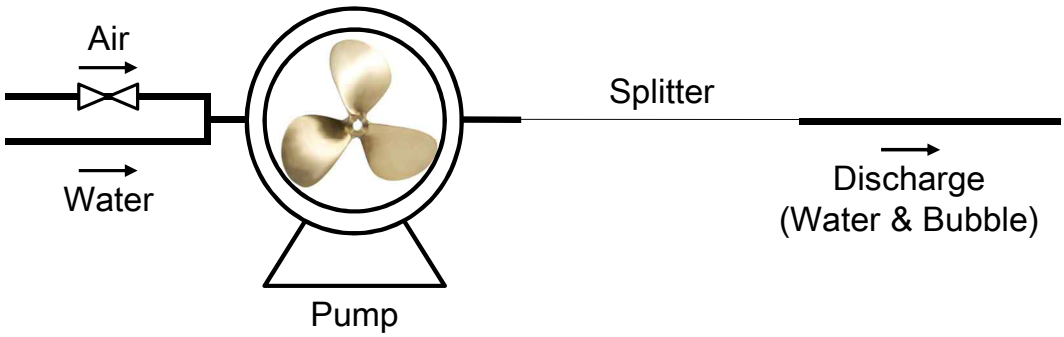

Fig. 2.3 Schematic diagram of
splitting-type fine bubble generator (Kim, 2014)

Water and air are driven into the splitter using a pump. As the mixture of water and air moves through the pipe, the shear force that the pipe wall exerts on passing bubbles splits the bubbles into smaller ones (Fig. 2.4). It was found that the

average diameter of the bubbles generated by the developed splitting-type generator was a few hundred nanometer (Kim, 2014).

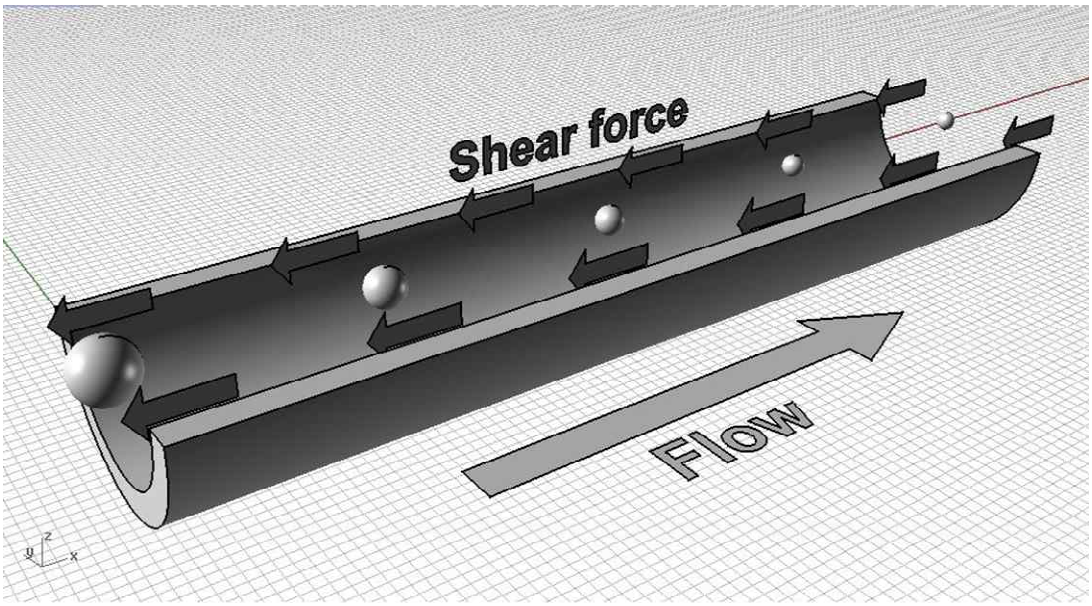

Fig. 2.4 Principle of splitting-type bubble generator

2.2 Helical pipe flow

Grindley and Gibson (1908) studied the effect of helical geometry on the frictional resistances to the flow of air by performing an experiment using a coiled pipe. Wang (1981) used a non-orthogonal helical coordinate system to analyze the effect of torsion and curvature in a helical pipe. Germano (1982) used an orthogonal helical coordinate system to analyze the helical pipe flow. Berger, Talbot, and Yao (1983) extensively reviewed studies on flow in curved pipes. Kao (1987) studied the torsion effect on a fully developed pipe in a helical pipe. Yamamoto, Yanase, and

Yoshida (1994) investigated the torsion effect on the flow patterns in a helical pipe. Gammack and Hydon (2001) found that the wall shear stress increased with the introduction of torsion.

The curvature and torsion of a helical pipe are defined as shown in Eq. (2.1) and Eq. (2.2).

$$\kappa = \frac{R}{R^2 + P^2} \qquad \text{Eq. (2.1)}$$

$$\tau = \frac{P}{R^2 + P^2} \qquad \text{Eq. (2.2)}$$

In these equations, R refers to the radius of the helix and P refers to the width of one complete helix turn that is measured parallel to the axis of the helix, as shown in Fig. 2.5.

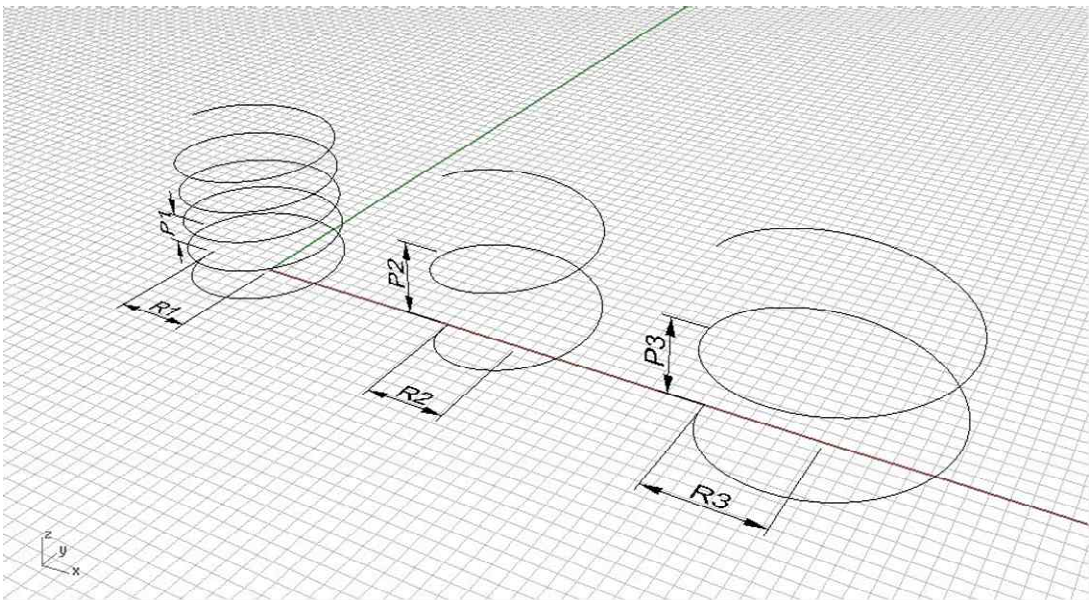

Fig. 2.5 Helical radius (R) and pitch (P)

Fig. 2.6 describes the velocity profile of a developing flow and a fully-developed flow in a pipe flow (Munson, Young, Okiishi, and Huebsch, 2009). The developing flow occurs at the curve and has an asymmetric velocity profile, attempting to balance it during the flow. The point at which the maximum axial velocity occurs is forced towards the outer wall in the developing flows. It was observed that a continuously developing flow occurs in a helical pipe.

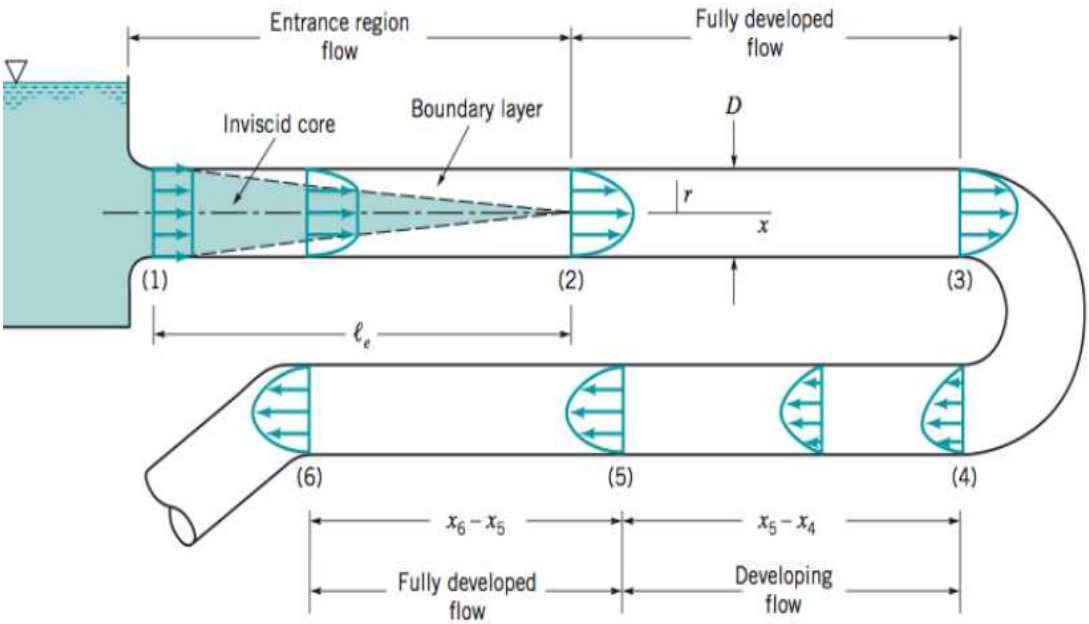

Fig. 2.6 Developing flow and fully-developed flow (Munson et al., 2009)

2.3 Three-dimensional (3D) printing

Three-dimensional (3D) printing, which is also known as additive manufacturing, is a technology that is used to create physical objects by depositing materials layer-by-layer. 3D printing has various advantages such as precise fabrication,

shortened production process, and reduced labor cost (Berman, 2012). A futurologist, Jeremy Rifkin (2011), discussed the possibility of enhanced energy efficiency that results from the energy saved at every step of the digital manufacturing process, from a reduction in the materials used to reduced energy expended to make the product.

The first 3D printing technology was developed by Chuck Hull in 1984 (Melchels, 2012). While traditional computer numerical control (CNC) uses subtractive manufacturing, which refers to the cutting away of material from a solid piece to create an object, 3D printing creates an object by building up layers of material.

Fig. 2.7 Difference of layer thickness (Cassaignau, 2015)

One of the most important aspects of 3D printing is the layer thickness, as shown in Fig. 2.7 (Sculpteo, 2015), which affects the qualities of products such as the production time, precision,

surface finish, and strength (Vaezi and Chua, 2011). Chua, Leong, and Lim (2010) extensively reviewed the principles and applications of 3D printing technologies. Table 2.1 shows several 3D printing technologies with their printing materials.

Table 2.1 3D printing technologies (Wikipedia, n.d.)

Type	Technologies	Materials
Extrusion	Fused-deposition modeling (FDM)	Thermoplastics, eutectic metals, edible materials, rubbers, modeling clay, plasticine, metal clay
	Fused filament fabrication (FFF)	
	Robocasting	Ceramic materials, metal alloy, cermet, metal matrix composite, ceramic matrix composite
	Direct ink writing (DIW)	
Light-polymerized	Stereolithography (SLA)	Photopolymer
	Digital light processing (DLP)	Photopolymer
Powder bed	Powder bed and inkjet head 3D printing (3DP)	Metal alloy, powdered polymers, plaster
	Electron-beam melting (EBM)	Metal alloy (including titanium alloys)
	Selective laser melting (SLM)	Titanium alloys, cobalt chrome alloys, stainless steel, aluminium
	Selective heat sintering (SHS)	Thermoplastic powder
	Selective laser sintering (SLS)	Thermoplastics, metal powders, ceramic powders
	Direct metal laser sintering (DMLS)	Metal alloy
Laminated	Laminated object manufacturing (LOM)	Paper, metal foil, plastic film
Wire	Electron beam freeform fabrication (EBF3)	Metal alloy

Chapter 3. Effect of Design Factors of Straight-pipe Splitter on Bubble Generation

The effect of design factors of a straight-pipe splitter on bubble generation was analyzed using both modeling and experiments. In Chapter 3.1, as a first step, the design factors of a straight-pipe splitter are defined. In Chapter 3.2, the predicted shear forces exerted on pipe flow are calculated using computational fluid dynamics (CFD) modeling. Because shear force is known to contribute to bubble splitting, there is a negative relationship between shear force and bubble size. In Chapter 3.3, the measured dissolved oxygen (DO) concentrations in the discharged outflow are measured. Earlier studies have found that measured DO concentration is negatively related to bubble size (Kim, 2014). In Chapter 3.4, the trends of shear forces and measured DO concentrations are compared and analyzed.

3.1 Determination of straight-pipe's design factors

In a previous study, Kim (2014) considered pipe length (L), pipe diameter (D), and Manning' s coefficient of roughness (f) as the design factors of a straight-pipe splitter.

In this study, the same factors were adopted for modeling and experiment. Fig. 3.1 illustrates the three design factors of a straight-pipe splitter.

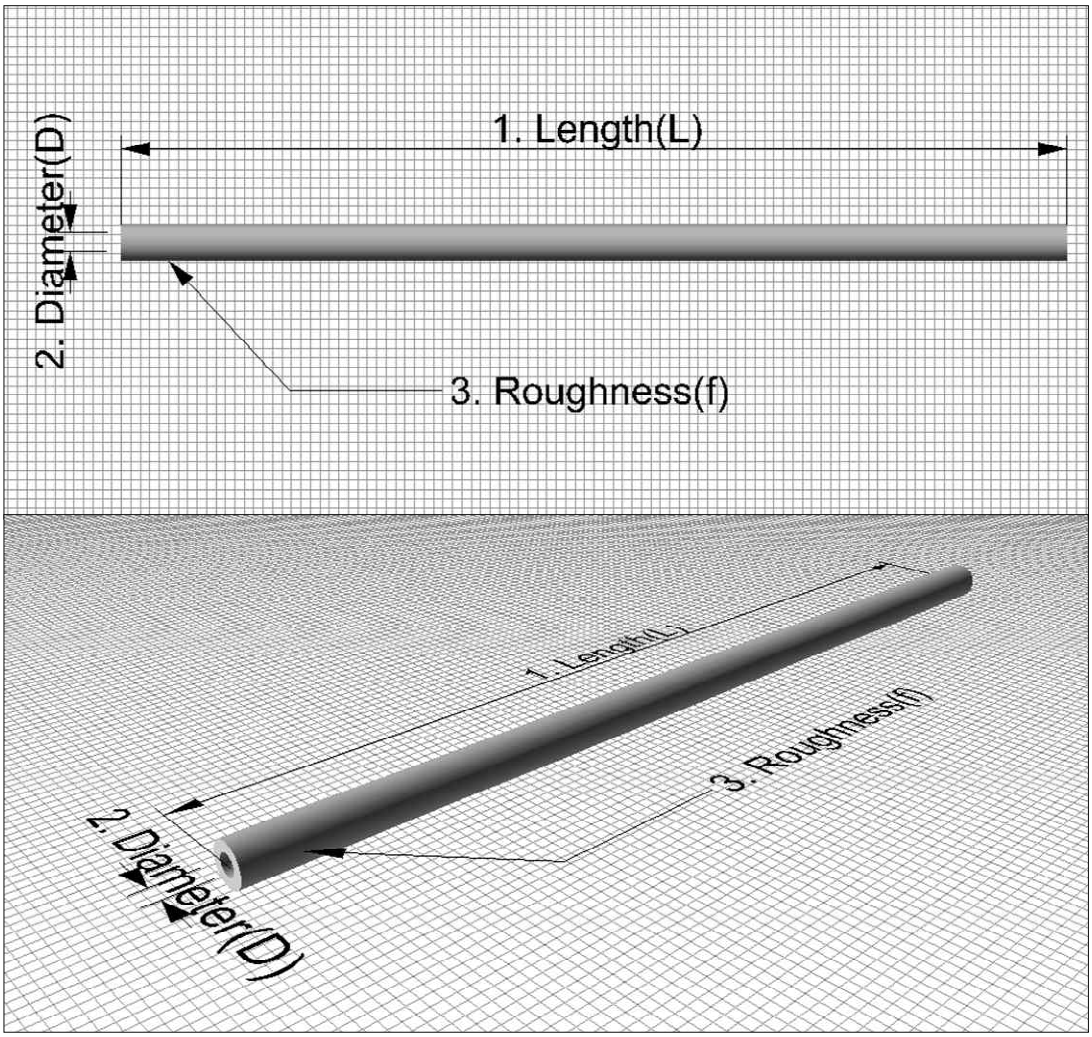

Fig. 3.1 Design factors of straight-pipe splitter:
Length (L), Diameter (D), Roughness (f)

In order to observe the individual effect of each design factor, a standard condition described in Table. 3.1 was set up. Then, modeling and experiments were conducted by varying each factor (L, D, f) individually.

Table 3.1 Standard conditions for straight-pipe splitter

Length (m)	Diameter (mm)	Roughness ($s/m^{1/3}$)
5	2	0.010

3.2 Shear force modeling on straight-pipe splitter

3.2.1 Modeling materials and methods

The predicted shear forces were calculated using CFD modeling. CFD is a widely used analysis tool that uses numerical analysis and algorithms to analyze problems of fluid flow, including pipe flow. In this study, OpenFOAM (Open source Field Operation and Manipulation) was used as a numerical solver to predict the shear force based on the variations of design factors of a straight-pipe splitter. A three-dimensional, $k-\omega$ turbulent model was used to simulate pipe flow in straight-pipe splitters. A single-phase flow was considered, and water was assumed to be incompressible. The shear force exerted on water during its passage through the pipe was calculated using the product of the surface area of the pipe and the average wall shear stress. Table 3.2 and Table 3.3 list the modeling conditions and schedule, respectively.

Table 3.2 Modeling conditions of straight-pipe splitter

Item	Condition
Program	OpenFOAM
Model	$k-\omega$ turbulent model
Compressibility	Incompressible water
Phase	Water (Single-phase)
Water flow rate	400 mL/min
Measurement	Shear force (N)

Table 3.3 Modeling schedule of straight-pipe splitter

No.	L (m)	D (mm)	f ($s/m^{1/3}$)	Remark
1	5	2	0.010	Standard
2	10	2	0.010	L-changed
3	5	4	0.010	D-changed
4	5	2	0.012	f-changed

3.2.2 Modeling results

Table 3.4 displays the results of shear force modeling based on variations of the design factors of the straight-pipe splitter. The shear force in model number 1, which was set up as a standard condition for straight-pipe splitters, was 0.80 N. The

shear force in model number 2, in which the length of the splitter was increased by 200%, was 5.04 N. The shear force in model number 3, in which the diameter of the splitter was increased by 200%, was 0.56 N. The shear force in model number 4, in which the Manning's coefficient of roughness was increased by 120%, was 1.26 N.

From the results of shear force modeling, it could be interpreted that the length (L) and roughness (f) of the splitter have a positive correlation with the shear force, and that diameter(D) has a negative correlation with the shear force. These trends show good agreement with the experimental results of Kim (2014).

Table 3.4 Summary of modeling results for straight-pipe splitters

No.	L (m)	D (mm)	f ($s/m^{1/3}$)	Remark	Shear force (N)
1	5	2	0.010	Standard	0.80
2	10	2	0.010	L-changed	5.04
3	5	4	0.010	D-changed	0.56
4	5	2	0.012	f-changed	1.26

3.3 DO concentration experiment on straight-pipe splitter

3.3.1 Experiment materials and methods

The equipment used in the experiment consisted of two pumps, splitters, a portable DO meter, water bath, timer, and a few piping parts such as reducers, I-fittings, and L-fittings. The two pumps used in this experiment had the same specifications: a discharge rate of 400 mL/min and a discharge pressure of 3 bar. Two different types of hoses were used for the splitters: silicon hoses with a Manning's coefficient of roughness of 0.010, and teflon hoses with a Manning's coefficient of roughness of 0.012. Fig. 3.2 shows the materials used for the splitters.

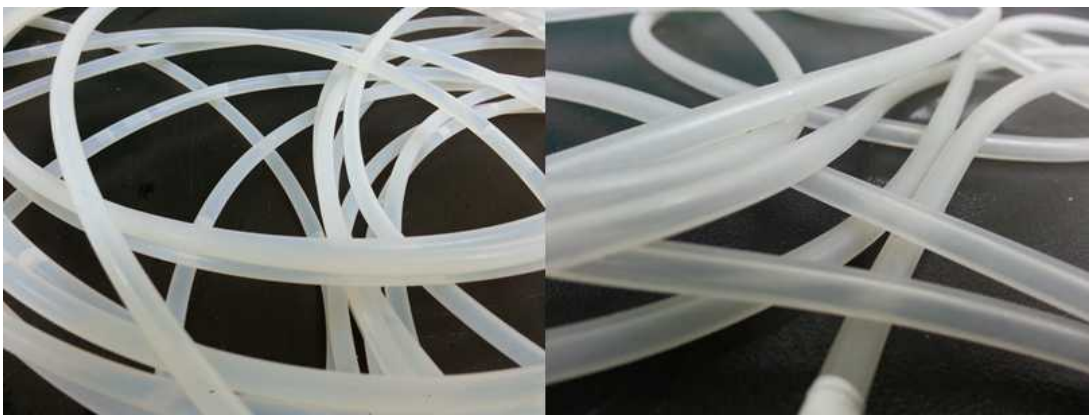

Fig. 3.2 Materials used for straight-pipe splitters: Silicon hose (left) and teflon hose (right)

Tap water and air were used as injected ingredients for bubble generation. The water bath had a dimension of 295 × 240 ×

150 mm. Fig. 3.3 shows the portable DO meter (ProODO, YSI) used for measuring DO concentration of discharged flow from the bubble generator.

Fig. 3.3 Portable DO meter

Fig. 3.4 describes the schematic diagram of the experiment. At the start of the experiment, tap water and air are drawn into the generator by the suction power of the pump. The pump's impeller mixes water and air while they are being injected into the splitter, and generates large bubbles. Then, the generated large bubbles are subjected to the shear force of the pipe splitter, and split into smaller bubbles continuously until they become sufficiently fine. When the water containing the split bubbles are discharged from the outlet to the water bath, the DO concentration is measured by the DO meter placed in the middle of the water bath. The designated dashed line represents the position where the straight-pipe splitters are connected.

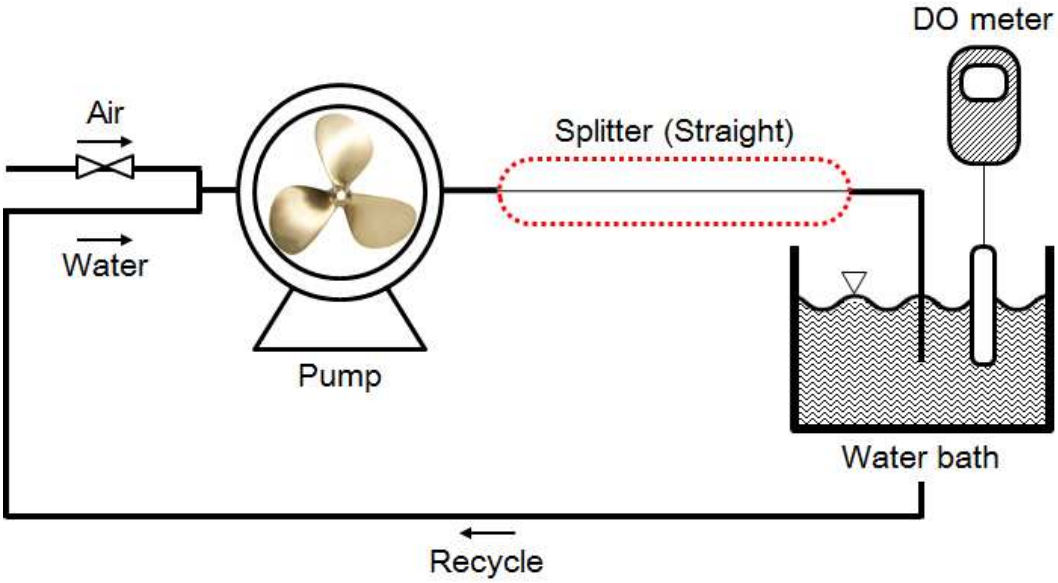

Fig. 3.4 Schematic diagram of DO measurement experiment of straight-pipe splitter

The DO concentration was measured for 60 min. During the first 10 min, when the variation was volatile, the DO concentration was measured in 1-min intervals. During the remaining 50 min, it was measured in 5-min intervals. Most of the experimental results showed that the DO concentration rapidly increased at the initial stage and was constant after reaching a certain point. This DO concentration was recorded as the final DO value.

Tables 3.5 and 3.6 display the experimental conditions and schedule, respectively. The variations of design factors considered were the same as in the modeling described in Chapter 3.2.

Table 3.5 Experimental conditions of straight-pipe splitter

Item	Condition
Temperature	16.7-18.4 ℃
Water flow rate	400-750 mL/min
Air flow rate	50-150 mL/min
Measuring device	YSI ProODO
Measurement	DO concentration (mg/L)

Table 3.6 Experimental schedule of straight-pipe splitter

No.	L (m)	D (mm)	f ($s/m^{1/3}$)	Remark
1	5	2	0.010	Standard
2	10	2	0.010	L-changed
3	5	4	0.010	D-changed
4	5	2	0.012	f-changed

3.3.2 Experiment results

The DO concentration in experiment number 1, which was set up as a standard condition, was 13.81 mg/L. In experiment number 2, the length of the splitter was increased by 200%, and the DO concentration was 15.77 mg/L. The DO concentrations in experiment number 3, in which the diameter of the splitter was

increased by 200%, and experiment number 4, in which the roughness of the splitter was increased by 120%, were 9.71 mg/L and 15.23 mg/L, respectively.

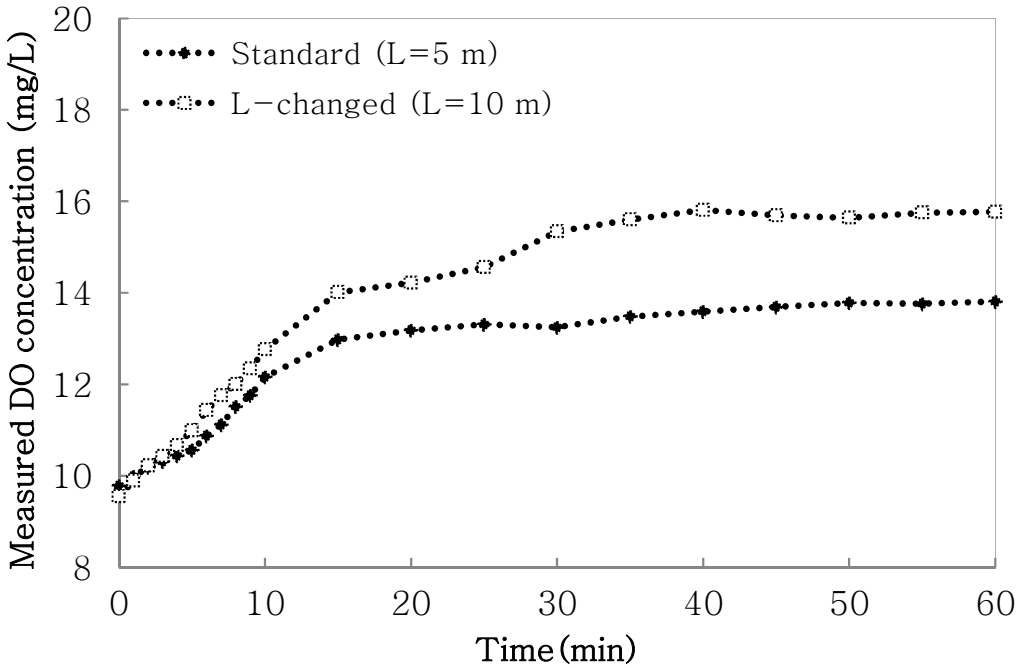

Fig. 3.5 Effect of straight pipe's length (L) on measured DO concentration

Fig. 3.5 shows the effect of the length of the straight pipe on the measured DO concentration. The DO concentrations of a 5-m and 10-m straight pipe were compared. The two curves showed similar trends of increasing over time in the first 40 min and becoming constant thereafter. The initial DO concentration of the two curves were 9.78 mg/L and 9.55 mg/L, respectively. The final DO concentrations were 13.81 mg/L and 15.77 mg/L, respectively.

These results indicate that the DO concentration increases with increasing the length of the straight pipe. The reason behind this tendency may be that bubbles have a greater chance of splitting because of the elongated length. The experimental results are consistent with the earlier prediction by CFD modeling that shear force increases with increasing pipe length.

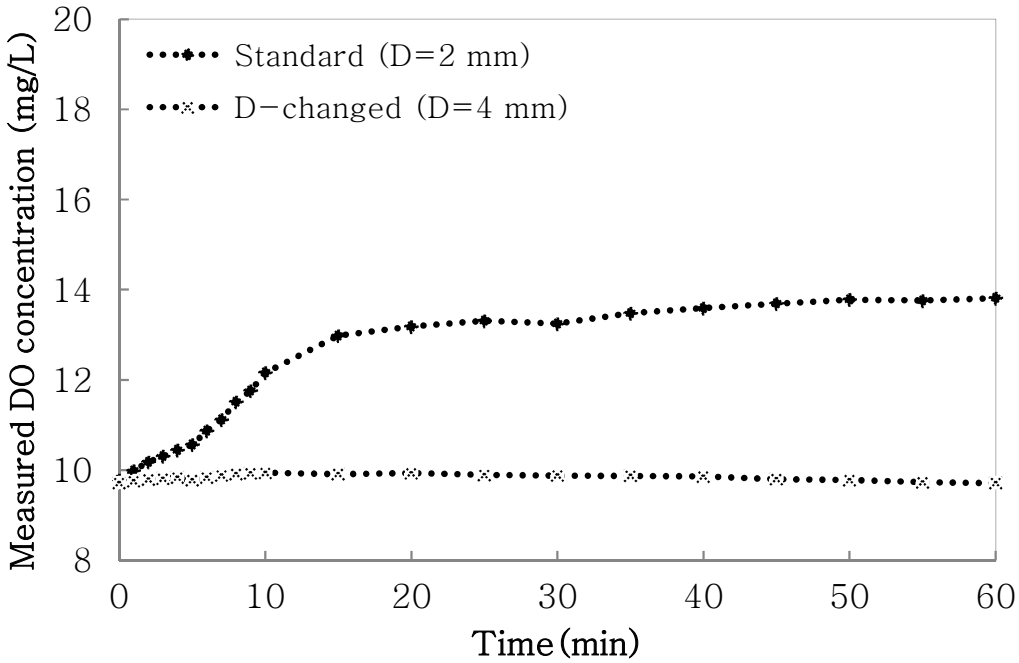

Fig. 3.6 Effect of straight pipe's diameter (D) on measured DO concentration

Fig. 3.6 shows the effect of the diameter of the straight pipe on the measured DO concentration. The DO concentrations of 2-mm-diameter and 4-mm-diameter straight pipes were compared. The two curves showed different trends. The DO concentration of the 4-mm-diameter straight pipe was constant

during the experiment. The initial DO concentrations of the two curves were 9.78 mg/L and 9.71 mg/L, respectively. The final DO concentrations were 13.81 mg/L and 9.71 mg/L, respectively.

These results indicate that, at a fixed flow rate, the DO concentration decreases with increasing diameter. This may be due to the fact that increasing the diameter at a fixed flow rate may decrease the velocity of pipe flow, thereby reducing the shear force. The experimental results are consistent with the earlier prediction by CFD modeling that shear force decreases with increasing pipe diameter.

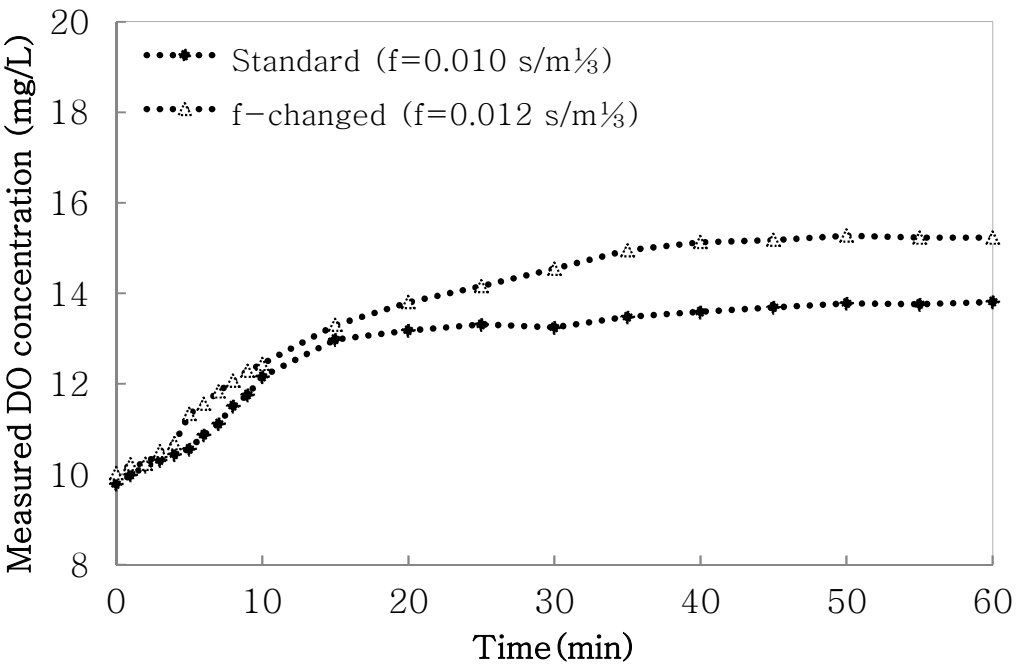

Fig. 3.7 Effect of straight pipe's roughness (f) on measured DO concentration

Fig. 3.7 shows the effect of the roughness of the straight pipe on the measured DO concentration. Straight pipes with roughness

values of 0.010 $s/m^{1/3}$ and 0.012 $s/m^{1/3}$ were compared. The two curves showed similar trends of increasing over time in the first 50 min and then becoming constant thereafter. The initial DO concentrations of the two curves were 9.78 mg/L and 10.02 mg/L, respectively. The final DO concentrations were 13.81 mg/L and 15.23 mg/L, respectively.

These results indicate that the DO concentration increases with increasing roughness. This may be due to the fact that rough surfaces exert higher shear forces on the passing bubbles. The experimental results are consistent with the earlier prediction by CFD modeling that shear force increases with increasing surface roughness.

Table 3.7 Summary of experimental results for straight-pipe splitters

No.	L (m)	D (mm)	f ($s/m^{1/3}$)	Remark	DO (mg/L)
1	5	2	0.010	Standard	13.81
2	10	2	0.010	L-changed	15.77
3	5	4	0.010	D-changed	9.71
4	5	2	0.012	f-changed	15.23

Table 3.7 shows the measured DO concentrations for each experiment based on variations of the design factors of the straight-pipe splitter. From the results of the experiments, it can be concluded that the length (L) and roughness (f) of the splitter show a positive correlation with the DO concentration of

the discharged outflow, and that the diameter (D) shows a negative correlation with the DO concentration of the discharged outflow. All these findings are consistent with the earlier prediction by CFD modeling in Chapter 3.2 as well as with the experimental results of Kim (2014).

3.4 Trends of modeling and experimental results

Fig. 3.8 shows the predicted shear forces and the measured DO concentrations on the same plot. Modeling and experimental results show similar trends in all the four straight-pipe splitters. From this result, it appears that shear force is highly related to DO concentration.

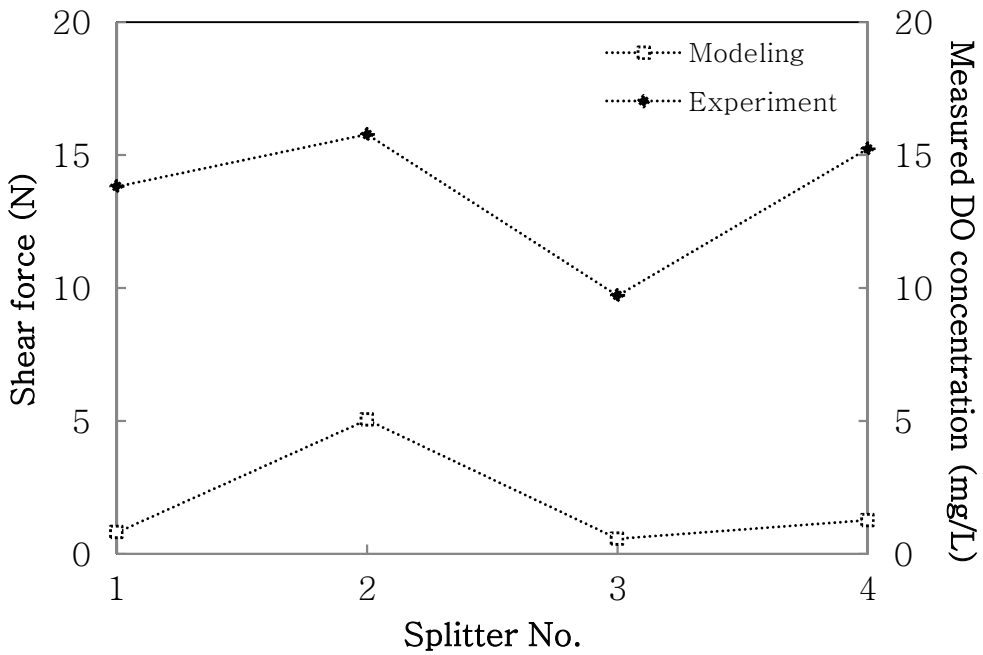

Fig. 3.8 Trends of modeling and experimental results for four straight-pipe splitters

Chapter 4. Effect of Design Factors of helical-pipe splitter on Bubble Generation

From the results of Chapter 3, it was observed that the shear force and DO concentration increase with increasing length of the straight-pipe splitter. For higher efficiency, however, a helical pipe can be used as an alternative to a straight pipe. Gammack and Hydon (2001) suggested that the wall shear stress increased because of the introduction of torsion in helical pipe flows, which breaks the symmetric structure and skews the velocity profiles. Motivated by their previous research, a helical pipe was used instead of a straight pipe in the splitters of a bubble generator. Furthermore, a helical pipe can reduce the volume of the splitter for extensive industrial applicability.

The effect of the design factors of a helical-pipe splitter was analyzed using the same method as that used for the straight-pipe splitter. In Chapter 4.1, the design factors of a helical-pipe splitter are defined. In Chapter 4.2, the predicted shear forces exerted on water are calculated by CFD modeling. In Chapter 4.3, the measured DO concentrations of the discharged outflow are measured. In Chapter 4.4, the trends of shear forces and measured DO concentration are compared, and the relationship between these two parameters is correlated. In Chapter 4.5, the results of Chapters 3 and 4 are integrated, and the results of the straight-pipe splitter and helical-pipe splitter are compared.

4.1 Determination of helical-pipe's design factors

The pipe length (L), pipe diameter (D), and Manning's coefficient of roughness (f), helical radius (R), and pitch (P) were considered as the design factors for a helical-pipe splitter, as shown in Fig. 4.1. A helical-pipe is determined as one when the five elements were given, unless more complex structures such as tapering sections, inner structures in pipes are taken into account.

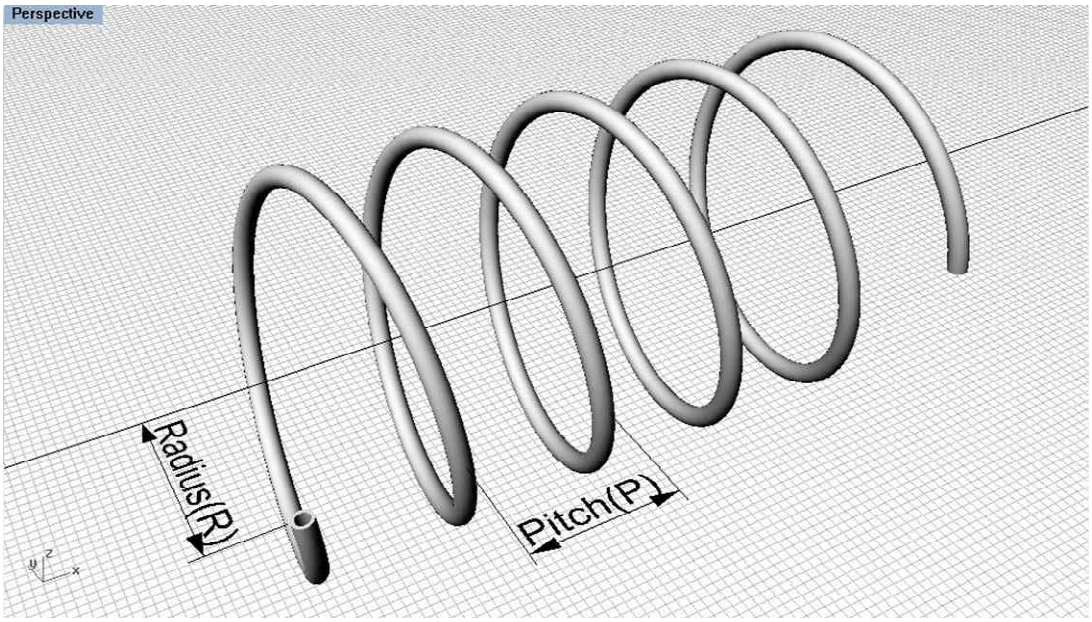

Fig. 4.1 Design factors of helical-pipe splitter

Length (L) denotes the total spiral length of the pipe centerline. Diameter (D) denotes the inner diameter of the pipe. Roughness (f) denotes the Manning's coefficient of roughness of the pipe surface. Radius (R) denotes the helical radius of the centerline. Pitch (P) denotes the direct distance between two

points when a point on the centerline returns to the same position after a circulation.

Table 4.1 Standard conditions for helical-pipe splitter

Length (m)	Diameter (mm)	Roughness ($s/m^{1/3}$)	Radius (mm)	Pitch (mm)
5	2	0.010	100	6

In order to observe the individual effect of each design factor, a standard condition described in Table. 4.1 was set up. Then, modeling and experiments were conducted by varying each factor (L, D, f, P, R) individually.

4.2 Shear force modeling on helical-pipe splitter

4.2.1 Modeling materials and methods

The effect of the design factors of a helical-pipe splitter on the predicted shear force was observed using CFD modeling. The modeling was conducted using the same method as that used for the straight-pipe splitter in Chapter 3.2. OpenFOAM, and a three-dimensional, $k-\omega$ turbulent model were used to simulate helical pipe flow. A single-phase flow was considered, and water was assumed to be incompressible. The shear force exerted on water during its passage through the pipe was calculated by the product of the surface area of the pipe and the average wall shear stress. Tables 4.2 and 4.3 list the modeling conditions and schedule, respectively.

Table 4.2 Modeling conditions of helical-pipe splitter

Item	Condition
Program	OpenFOAM
Model	$k-\omega$ turbulent model
Compressibility	Incompressible water
Phase	Water (Single-phase)
Water flow rate	400 mL/min
Measurement	Shear force (N)

Table 4.3 Modeling schedule of helical-pipe splitter

No.	L (m)	D (mm)	f ($s/m^{1/3}$)	R (mm)	P (mm)	Remark
5	10	2	0.010	100	6	Standard
6	5	2	0.010	100	6	L-changed
7	10	4	0.010	100	6	D-changed
8	10	2	0.012	100	6	f-changed
9	10	2	0.010	10	6	R-changed
10	10	2	0.010	100	12	P-changed

Figs. 4.2, 4.3, 4.4, 4.5, 4.6 and 4.7 show the geometries of each helical-pipe splitter. Tables 4.4 lists the conversion of R, P into κ, τ.

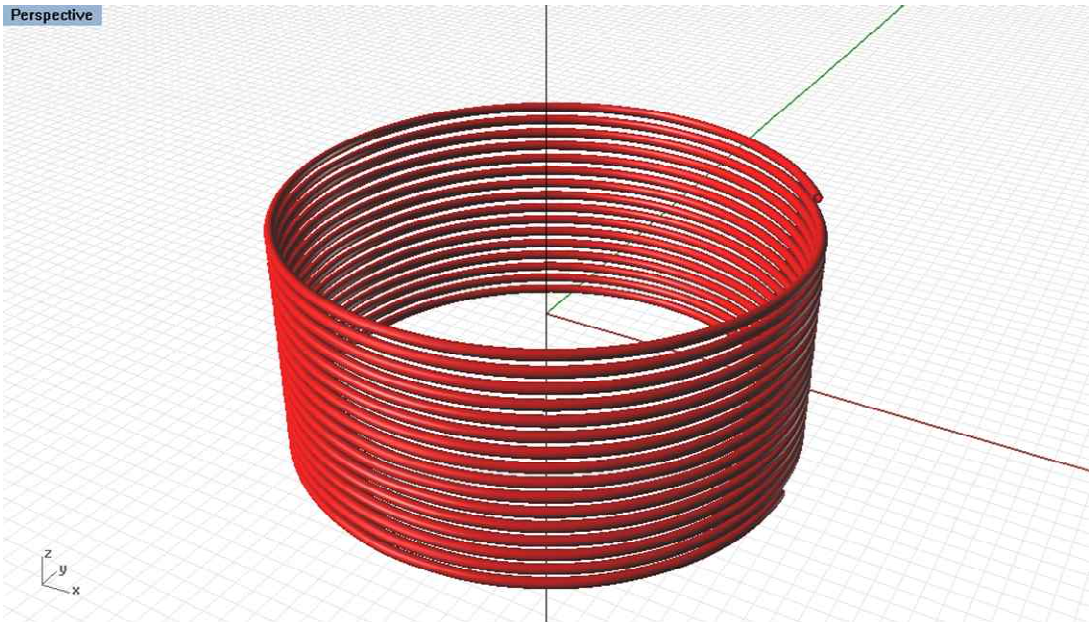

Fig. 4.2 Geometry of helical-pipe splitter No. 5
(Standard condition)

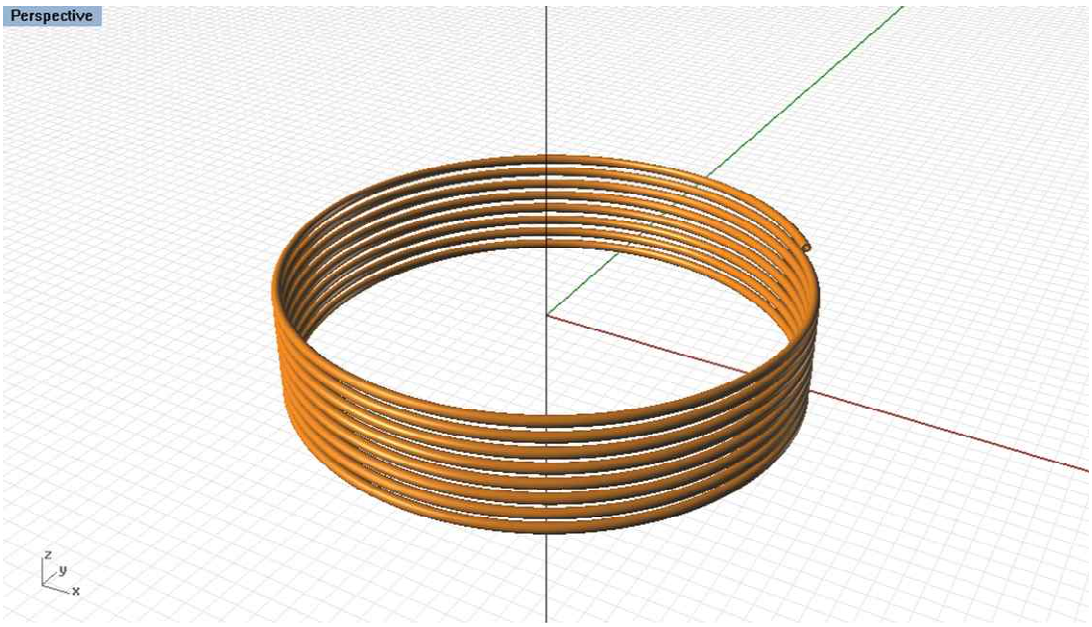

Fig. 4.3 Geometry of helical-pipe splitter No. 6
(L-changed)

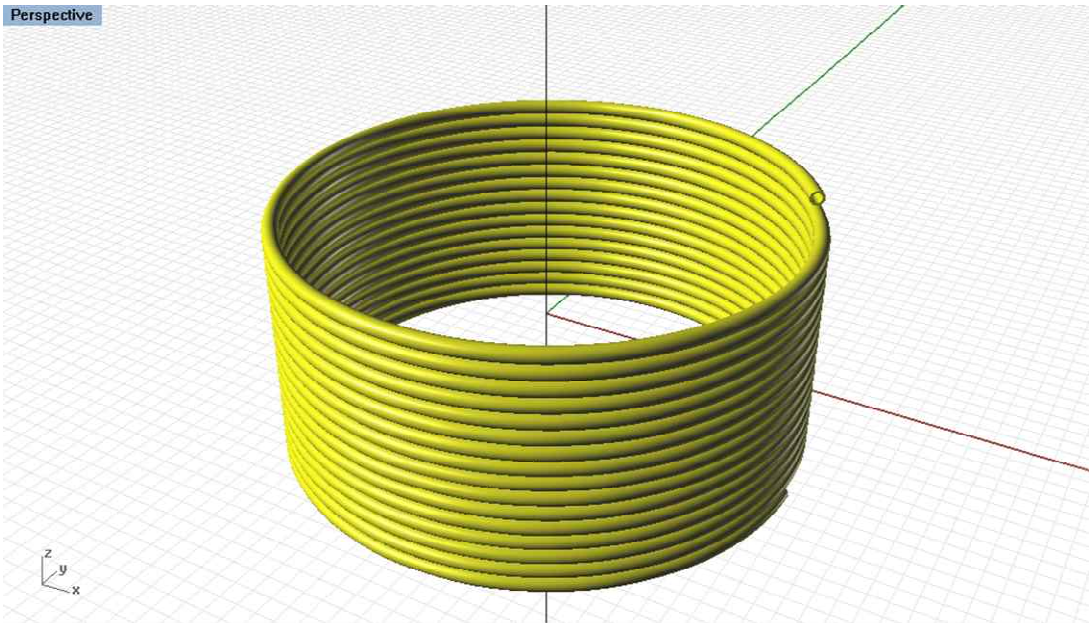

Fig. 4.4 Geometry of helical-pipe splitter No. 7
(D-changed)

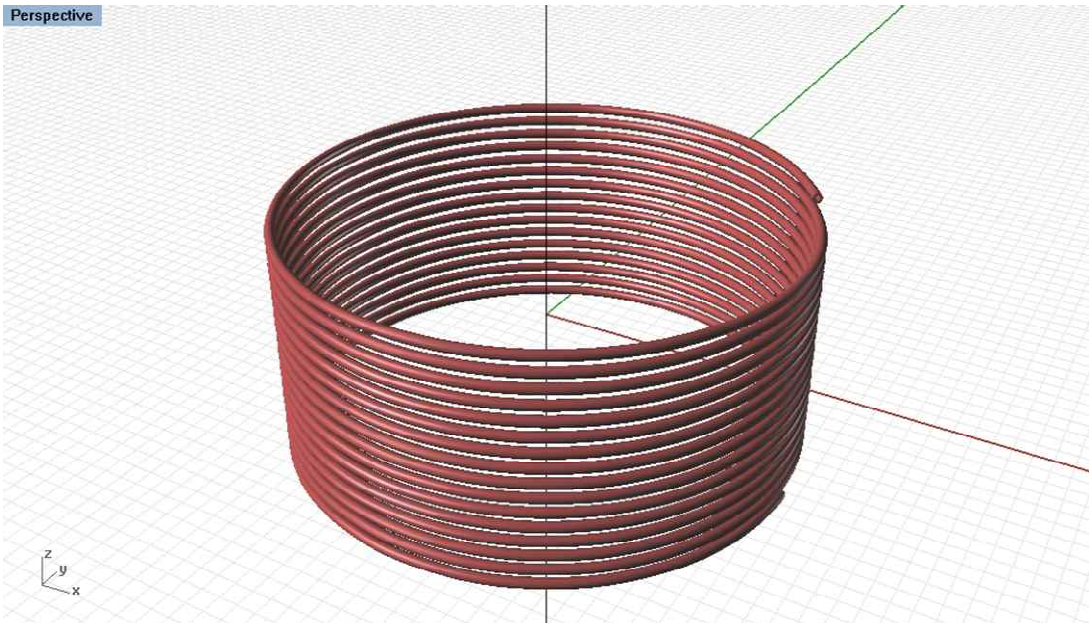

Fig. 4.5 Geometry of helical-pipe splitter No. 8
(f-changed)

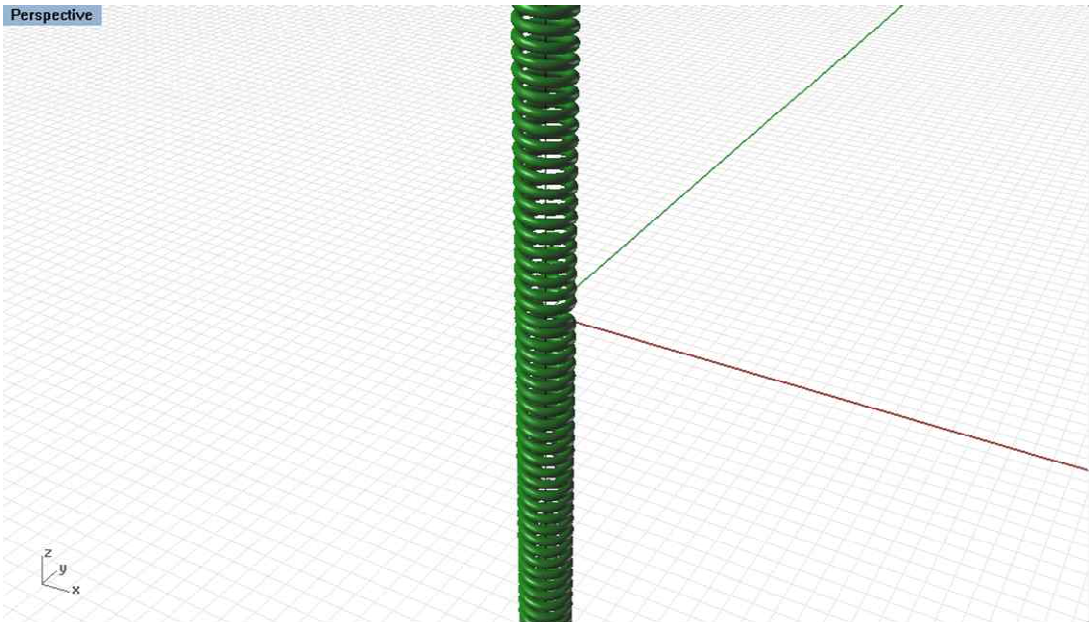

Fig. 4.6 Geometry of helical-pipe splitter No. 9
(R-changed)

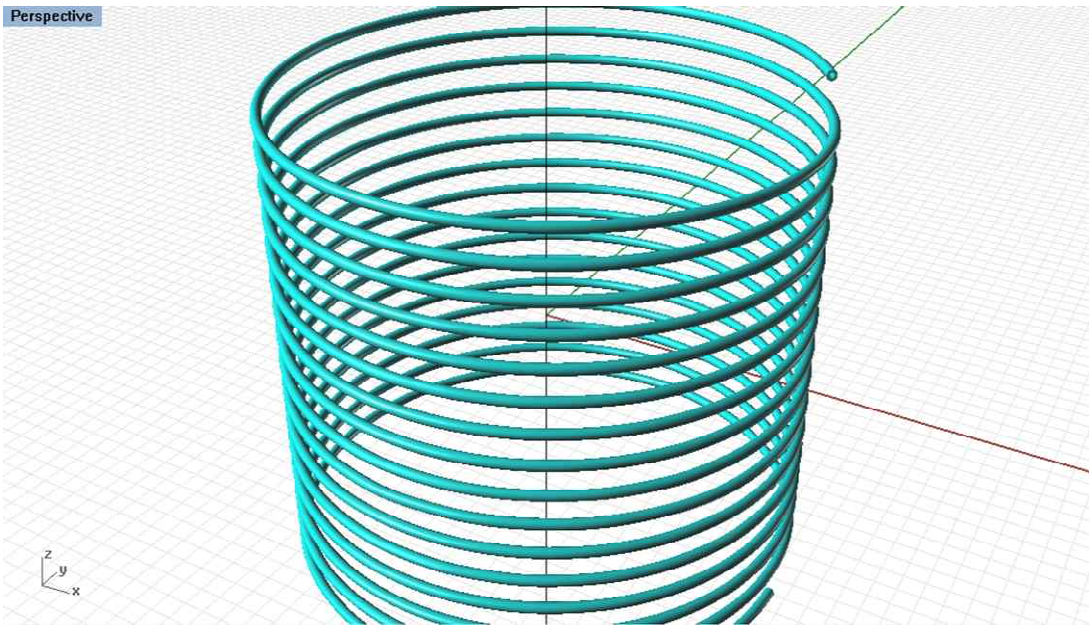

Fig. 4.7 Geometry of helical-pipe splitter No. 10
(P-changed)

Table 4.4 Conversion of R, P into κ, τ

No.	Helical radius (R)	Pitch (P)	Curvature (κ)	Torsion (τ)
5	100	6	0.0100	0.0006
6	100	6	0.0100	0.0006
7	100	6	0.0100	0.0006
8	100	6	0.0100	0.0006
9	10	6	0.0735	0.0441
10	100	12	0.0099	0.0012

4.2.2 Modeling results

Table 4.5 displays the results of shear force modeling based on variations of the design factors of the helical-pipe splitter. The shear force in model number 5, which was set up as a standard condition for the helical-pipe splitter, was 11.03 N. The length of the splitter was decreased by 50% in model number 6, and the corresponding shear force was 5.51 N. The shear forces in model number 7, in which the diameter of the splitter was increased by 200%, and in model number 8, in which increased the Manning's coefficient of roughness of the splitter was increased by 120%, were 3.60 N and 11.90 N, respectively. Decreasing the helical radius of the splitter by 10% in model number 9 resulted in a shear force of 14.40 N. The shear force in model number 10, in which the pitch of the splitter was increased by 200%, was 11.04 N.

Table 4.5 Summary of modeling results for helical-pipe splitters

No.	L (m)	D (mm)	f ($s/m^{1/3}$)	R (mm)	P (mm)	Remark	Shear force (N)
5	10	2	0.010	100	6	Standard	11.03
6	5	2	0.010	100	6	L-changed	5.51
7	10	4	0.010	100	6	D-changed	3.60
8	10	2	0.012	100	6	f-changed	11.90
9	10	2	0.010	10	6	R-changed	14.40
10	10	2	0.010	100	12	P-changed	11.04

From the results of the shear force modeling, it can be assumed that the length (L) and roughness (f) of the splitter show a positive correlation with the shear force, and that the diameter (D) and helical radius (R) show a negative correlation with the shear force. The pitch (P) of the helical pipe seems to have no relationship with the shear force.

4.3 DO concentration experiment on helical-pipe splitter

4.3.1 Experiment materials and methods

The same experimental set-up was used as that for the experiment of the straight-pipe splitter in Chapter 3.3. The geometry of the splitter was changed from straight to helical. Fig. 4.8 shows the two different helical-pipe splitters used in this experiment: Silicon hose (f=0.010 $s/m^{1/3}$) and teflon hose (f=0.012 $s/m^{1/3}$). These splitters were hose-coiled pipes with a helical radius of 10 mm and 100 mm.

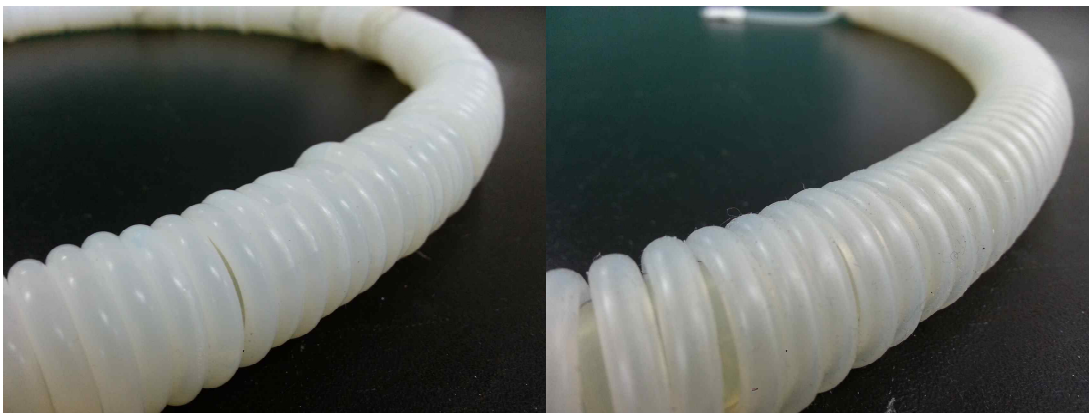

Fig. 4.8 Hose-coiled helical-pipe splitters:
Silicon hose (left) and teflon hose (right)

Fig. 4.9 describes the schematic diagram of the experiment. Tap water and air are drawn into the generator by the pump, and the mixture is split by the shear force of the pipe splitter. When the water containing the split bubbles are discharged from the outlet to the water bath, the DO concentration is measured

by the DO meter placed in the middle of the water bath. The designated dashed line represents the position of where the helical-pipe splitters are connected.

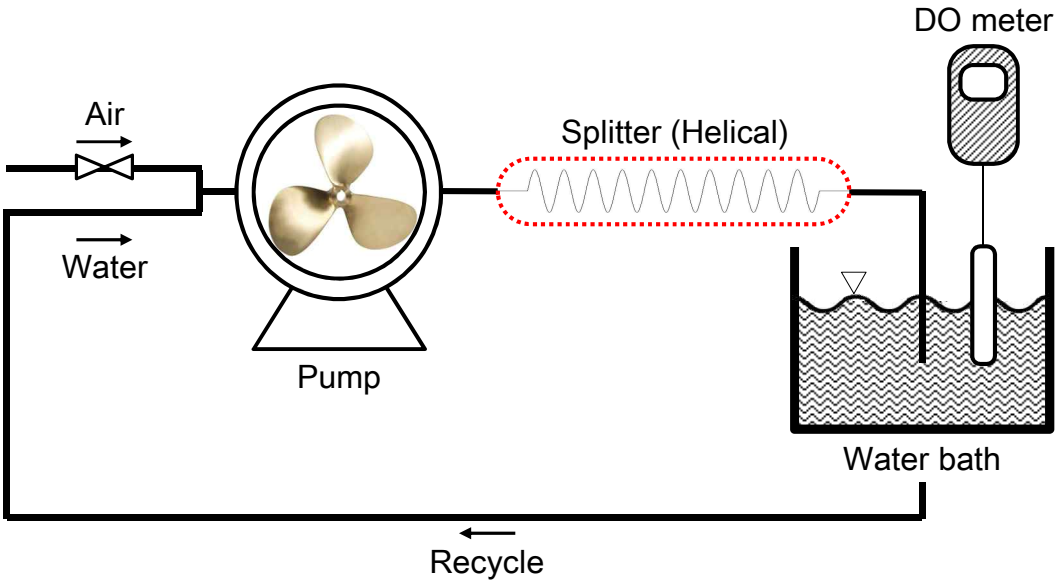

Fig. 4.9 Schematic diagram of DO measurement experiment of helical-pipe splitter

The DO concentration was measured for 60 min. The measurement was conducted at 1-min intervals for the first 10 min, and 5-min intervals for the remaining 50 min. Most of the experimental results showed a constant value after a certain point. This DO concentration was recorded as the final DO value.

Tables 4.6 and 4.7 list the experimental conditions and schedule, respectively. The variations of the design factors were the same as the modeling in Chapter 4.2.

Table 4.6 Experimental conditions of helical-pipe splitter

Item	Condition
Temperature	16.4-20.5 ℃
Water flow rate	400-750 mL/min
Air flow rate	50-150 mL/min
Measuring device	YSI ProODO
Measurement	DO concentration (mg/L)

Table 4.7 Experimental schedule of helical-pipe splitter

No.	L (m)	D (mm)	f ($s/m^{1/3}$)	R (mm)	P (mm)	Remark
5	10	2	0.010	100	6	Standard
6	5	2	0.010	100	6	L-changed
7	10	4	0.010	100	6	D-changed
8	10	2	0.012	100	6	f-changed
9	10	2	0.010	10	6	R-changed
10	10	2	0.010	100	12	P-changed

4.3.2 Experiment results

The DO concentration in experiment number 5, which was set up as a standard condition, was 16.04 mg/L. In experiment number 6, the length of the splitter was decreased by 50%, and the corresponding DO concentration was 14.17 mg/L. The diameter of the splitter was increased by 200% in experiment number 7, and the DO concentration was 11.05 mg/L. The DO concentration in experiment number 8, in which the Manning's coefficient of roughness of the splitter was increased by 120%, was 16.71 mg/L. The DO concentrations in experiment number 9, in which the helical radius of the splitter was decreased by 10%, was 17.53. In experiment number 10, the pitch of the splitter was increased by 200%, and the corresponding DO concentration was 15.92 mg/L.

Fig. 4.10 shows the effect of the length of the helical pipe on the measured DO concentration. Helical pipes having lengths of 10 m and 5 m were compared. The two curves showed similar trends of increasing over time in the first 45 min and were constant thereafter. The initial DO concentrations of the two curves were 9.45 mg/L and 9.71 mg/L, respectively. The final DO concentrations were 16.04 mg/L and 14.17 mg/L, respectively.

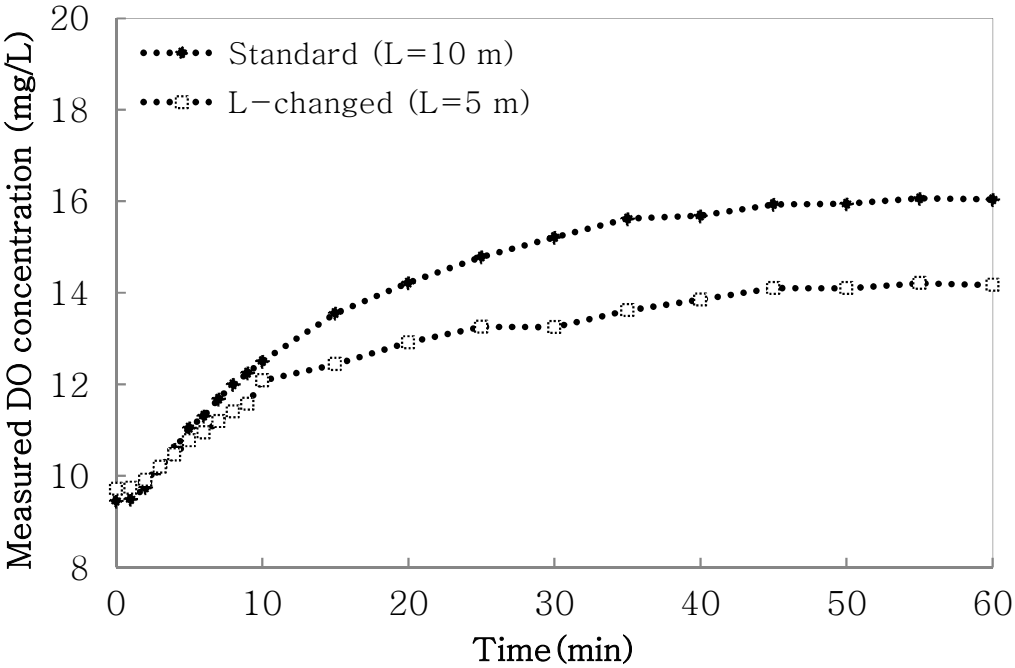

Fig. 4.10 Effect of helical pipe's length (L) on measured DO concentration

These results indicate that the DO concentration increases with increasing length, even in helical−pipe splitters. This may be due to the same reason that bubbles have a greater chance of splitting if the pipe is elongated, which contributes to generating smaller bubbles. The experiment result is consistent with the earlier prediction by CFD modeling that the shear force increases with increasing pipe length.

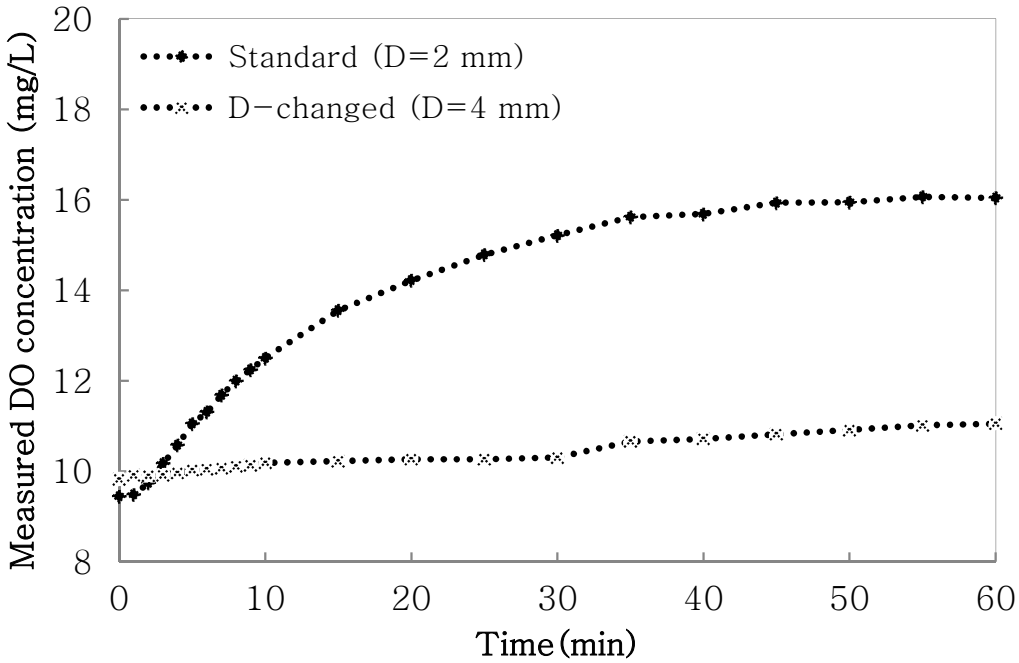

Fig. 4.11 Effect of helical pipe's diameter (D) on measured DO concentration

Fig. 4.11 shows the effect of the diameter of the helical−pipe splitter on the measured DO concentration. Helical pipes having diameters of 2 mm and 4 mm were compared. The two curves showed different trends. The DO concentration of the helical pipe having a 4−mm diameter slightly increased and was constant thereafter. The initial DO concentrations of the two curves were 9.45 mg/L and 9.82 mg/L, respectively. The final DO concentrations were 16.04 mg/L and 11.05 mg/L, respectively.

These results indicate that the DO concentration decreases with increasing diameter in helical−pipe splitters as well. This may be due to the same reason that increasing the diameter increases the cross−sectional area and decreases the velocity of

pipe-flow, which reduces the shear force. The experimental results are consistent with the earlier prediction by CFD modeling that shear force decreases with increasing pipe diameter.

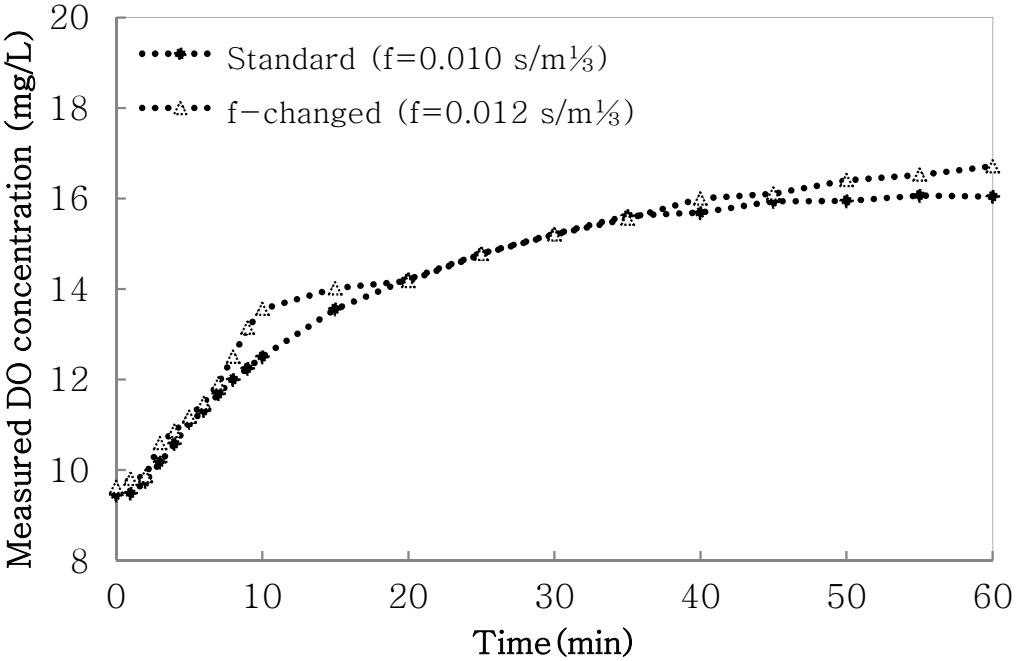

Fig. 4.12 Effect of helical pipe's roughness (f) on measured DO concentration

Fig. 4.12 shows the effect of the roughness of helical-pipe splitter on the measured DO concentration. Helical pipes having roughness values of 0.010 $s/m^{1/3}$ and 0.012 $s/m^{1/3}$ were compared. The two curves showed similar trends of increasing over time during the first 50 min and became constant thereafter. The initial DO concentrations of the two curves were 9.45 mg/L and 9.62 mg/L, respectively. The final DO concentrations were 16.04 mg/L and 16.71 mg/L, respectively.

These results indicate that the DO concentration increases with increasing roughness in helical-pipe splitters as well. This may be due to the fact that rough surfaces exert a higher shear force on the passing bubbles. The experimental results are consistent with the earlier prediction by CFD modeling that shear force increases with increasing surface roughness.

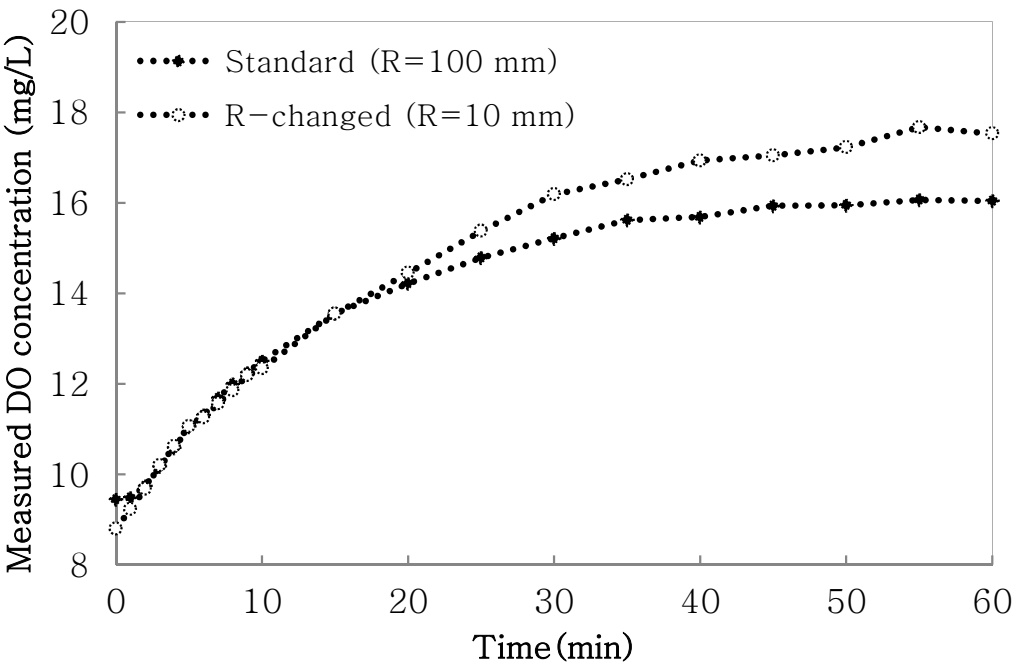

Fig. 4.13 Effect of helical pipe's helical radius (R) on measured DO concentration

Fig. 4.13 shows the effect of the helical radius of the helical-pipe splitter on the measured DO concentration. Helical pipes having helical radii of 100 mm 10 mm were compared. The two curves showed similar trends of increasing over time in the first 45 min and became constant thereafter. The initial DO concentrations of the two curves were 9.45 mg/L and 8.80 mg/L,

respectively. The final DO concentrations were 16.04 mg/L and 17.53 mg/L, respectively.

These results indicate that the DO concentration increases with decreasing helical radius. This may be attributed to torsion, which contributes toward increasing the wall shear stress with decreasing helical radius. The experiment results are consistent with the earlier prediction by CFD modeling that shear force increases with decreasing helical radius.

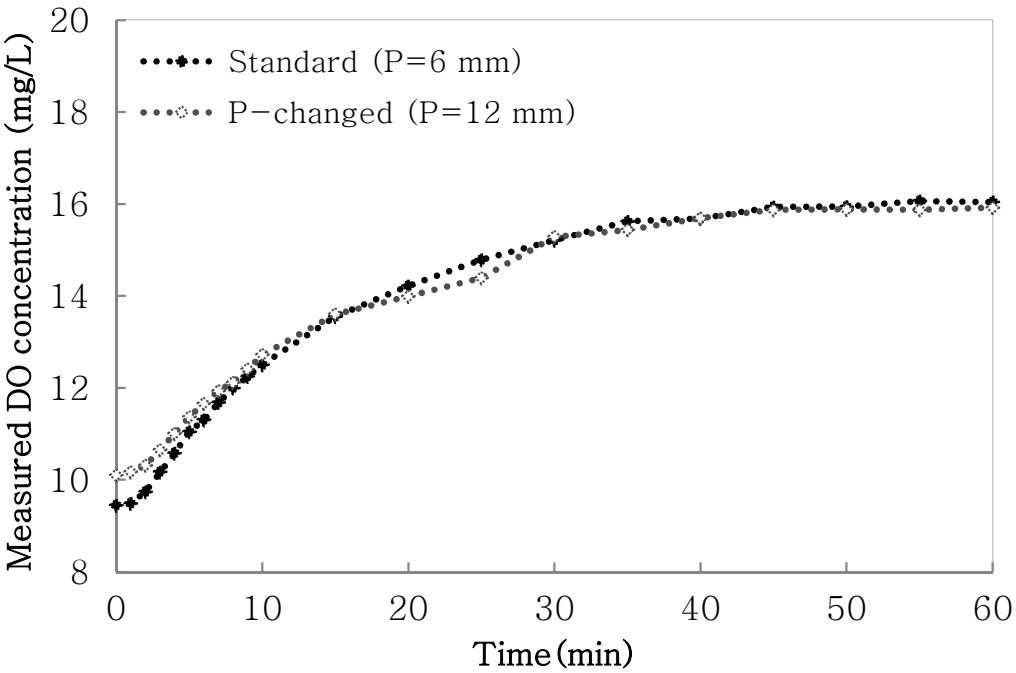

Fig. 4.14 Effect of helical pipe's pitch (P) on measured DO concentration

Fig. 4.14 shows the effect of the pitch of the helical−pipe splitter on the measured DO concentration. Helical pipes with pitches of 6 mm and 12 mm were compared. The two curves showed similar trends of increasing over time in the first 40 min

and became constant thereafter. The initial DO concentrations of the two curves were 9.45 mg/L and 10.01 mg/L, respectively. The final DO concentrations were 16.04 mg/L and 15.92 mg/L, respectively.

These results imply that the pitch does not influence the DO concentration. The experimental results are consistent with the earlier prediction by CFD modeling that the pitch has no relationship with the DO concentration.

Table 4.8 Summary of experimental results for helical-pipe splitters

No.	L (m)	D (mm)	f ($s/m^{1/3}$)	R (mm)	P (mm)	Remark	DO (mg/L)
5	10	2	0.010	100	6	Standard	16.04
6	5	2	0.010	100	6	L-changed	14.17
7	10	4	0.010	100	6	D-changed	11.05
8	10	2	0.012	100	6	f-changed	16.71
9	10	2	0.010	10	6	R-changed	17.53
10	10	2	0.010	100	12	P-changed	15.92

Table 4.8 summarizes the measured DO concentrations for each experiment based on variations of the design factors of the helical-pipe splitter. From the results of the experiments, it can be concluded that the length (L) and roughness (f) of the splitter show a positive correlation with the DO concentration of the discharged outflow, and that the diameter (D) and helical

radius (R) show a negative correlation with the DO concentration of the discharged outflow. The pitch (P) has no relationship with the DO concentration of the discharged outflow. All these findings are consistent with the earlier prediction by CFD modeling in Chapter 4.2.

4.4 Trends of modeling and experimental results

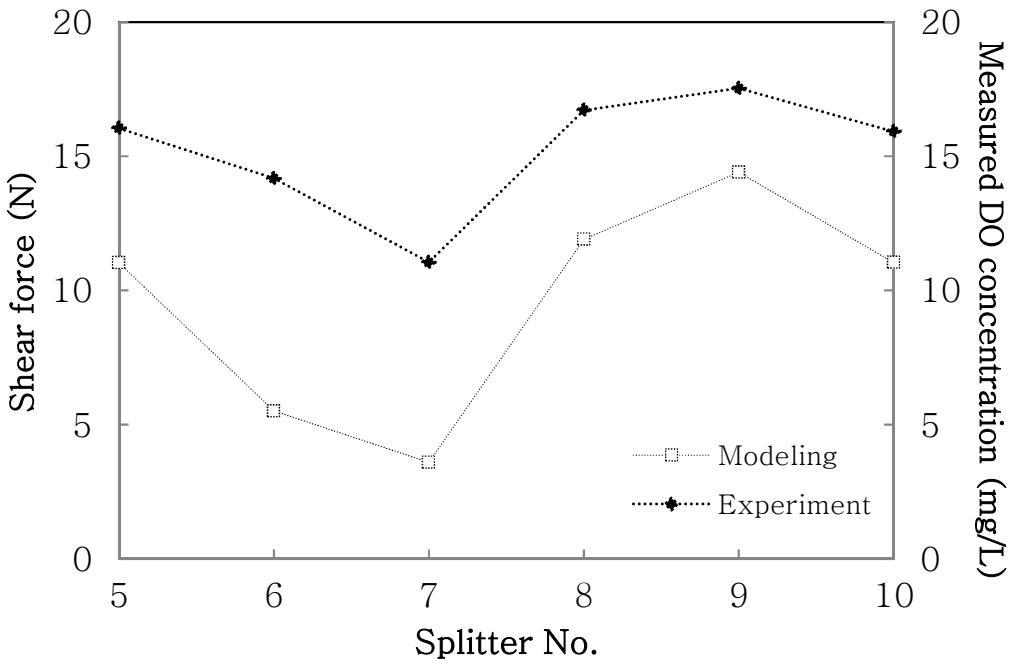

Fig. 4.15 Trends of modeling and experimental results for six helical-pipe splitters

Fig. 4.15 shows the predicted shear forces and the measured DO concentrations on the same plot. The modeling and experimental results show similar trends for all the six helical-pipe splitters. From these results, it appears that the shear force is highly related to the DO concentration.

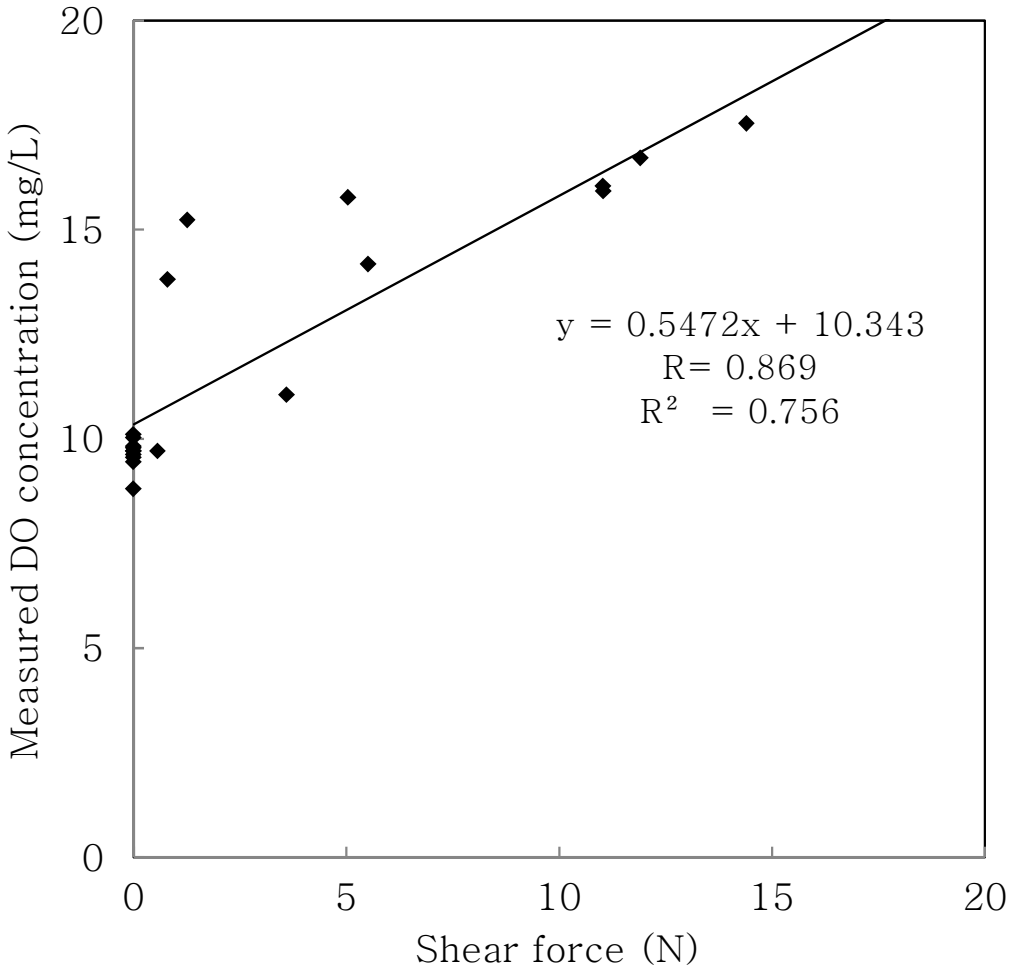

Fig. 4.16 Regression analysis of shear force and measured DO concentration

Fig. 4.16 represents the regression analysis of the shear force and the measured DO concentration. From the results of the 10 modeling and experimental sets, 20 data points were plotted. The gradient of linear regression was 0.5472, and the correlation coefficients R and R^2 were 0.869 and 0.756, respectively. Therefore, it can be inferred that the shear force is positively correlated with the DO concentration.

4.5 Comparison of straight-pipe and helical-pipe splitters

The straight-pipe splitter and helical-pipe splitter were compared. Table 4.9 lists the specifications of the two pipes. The straight pipe has no R and P values, while the values of R and P of the helical pipe are 10 mm and 6 mm, respectively. The values of the other design factors, i.e., L, D, and f, are the same for both the splitters.

Table 4.9 Properties of straight-pipe and helical-pipe splitters

Shape	L (m)	D (mm)	f ($s/m^{1/3}$)	R (mm)	P (mm)	Remark
Straight	10	2	0.010	-	-	No. 2
Helical	10	2	0.010	10	6	No. 9

Fig. 4.17 represents the effect of the straight-pipe and helical-pipe splitters on the shear force and DO concentration. The shear forces of the straight-pipe and helical-pipe splitters, obtained from CFD modeling, were 5.04 N and 14.40 N, respectively. The DO concentrations of the straight-pipe and helical-pipe splitters, obtained from the experiments, were 15.77 mg/L and 17.53 mg/L, respectively.

From these results, it is evident that helical-pipe splitters are more effective than straight-pipe splitters for increasing the shear force and DO concentration.

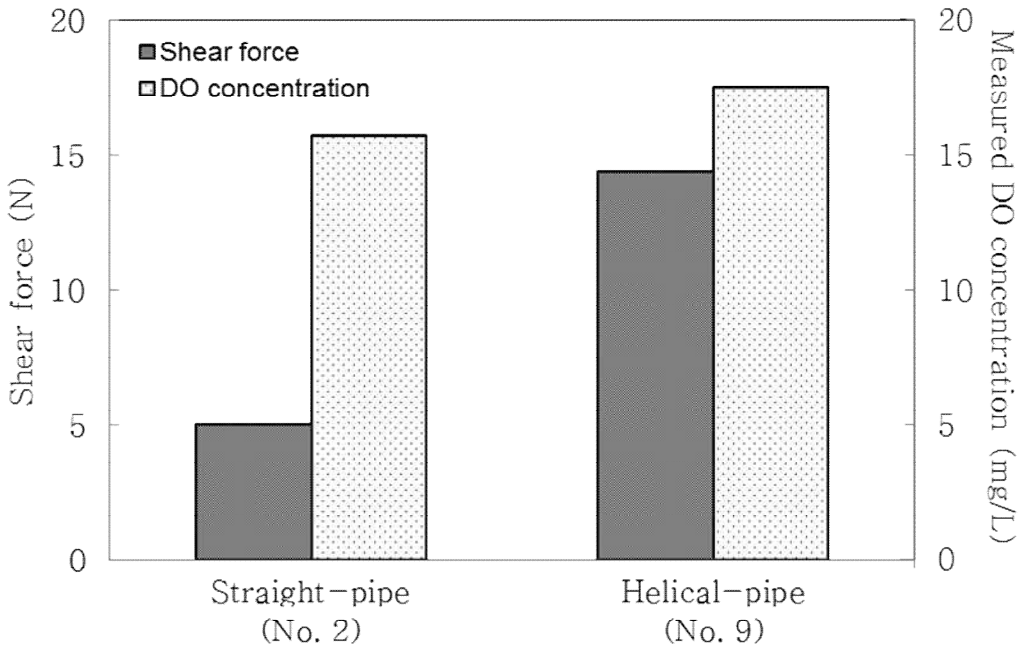

Fig. 4.17 Comparison of straight-pipe and helical-pipe splitters

Chapter 5. Miniaturization of helical-pipe splitter by 3D Printing

From the results of Chapter 3 and 4, it can be concluded that smaller helical radii and smaller diameters increase the shear force and DO concentration. Furthermore, the miniaturization of the splitter will increase the mobility of fine bubble generators by reducing their volume and mass, which can contribute to diverse industrial applications.

Therefore, the aim of this chapter is to determine an effective way to miniaturize splitters. In this regard, 3D printing, which builds an object by adding several layers of material having a thickness on the order of a few micrometers, can be used because miniaturization of the splitter of a bubble generator requires highly precise and elaborate fabrication.

In Chapter 5.1, the manufacturing process of a compact helical-pipe splitter by using 3D printing is described. Chapter 5.2 describes the DO concentration experiment conducted on a 3D-printed helical-pipe splitter. A comparison of the results with those obtained for the hose-coiled splitter is shown in Chapter 5.3. The volumes and masses of the helical-pipe and hose-coiled splitters are compared in Chapter 5.4.

5.1 Making process of 3D-printed helical-pipe splitter

5.1.1 Modeling

Rhinoceros 4.0 (Robert McNeel & Associates) was used for the modeling of a helical-pipe splitter. Rhinoceros is a 3D computer graphics and computer-aided design (CAD) application software widely used in the field of industrial design, which adopts non-uniform rational basis spline (NURBS) as a mathematical model for generating and representing curves and surfaces.

Fig. 5.1 illustrates the blueprints of the helical-pipe splitter from several points of view: perspective, top, left, and right. The length, diameter, helical radius, and pitch of the helical pipe are 2.5 m, 2 mm, 10 mm, and 3 mm, respectively. Overhanging pipes were placed at each end to increase the length by connecting more helical-pipe splitters in series. The volume and mass of the helical-pipe splitter can be reduced by decreasing the pitch by 50% (i.e., from 6 mm to 3 mm).

The thickness of each layer was 50 ㎛, and the completed design was saved in STL (STereoLithography) file format.

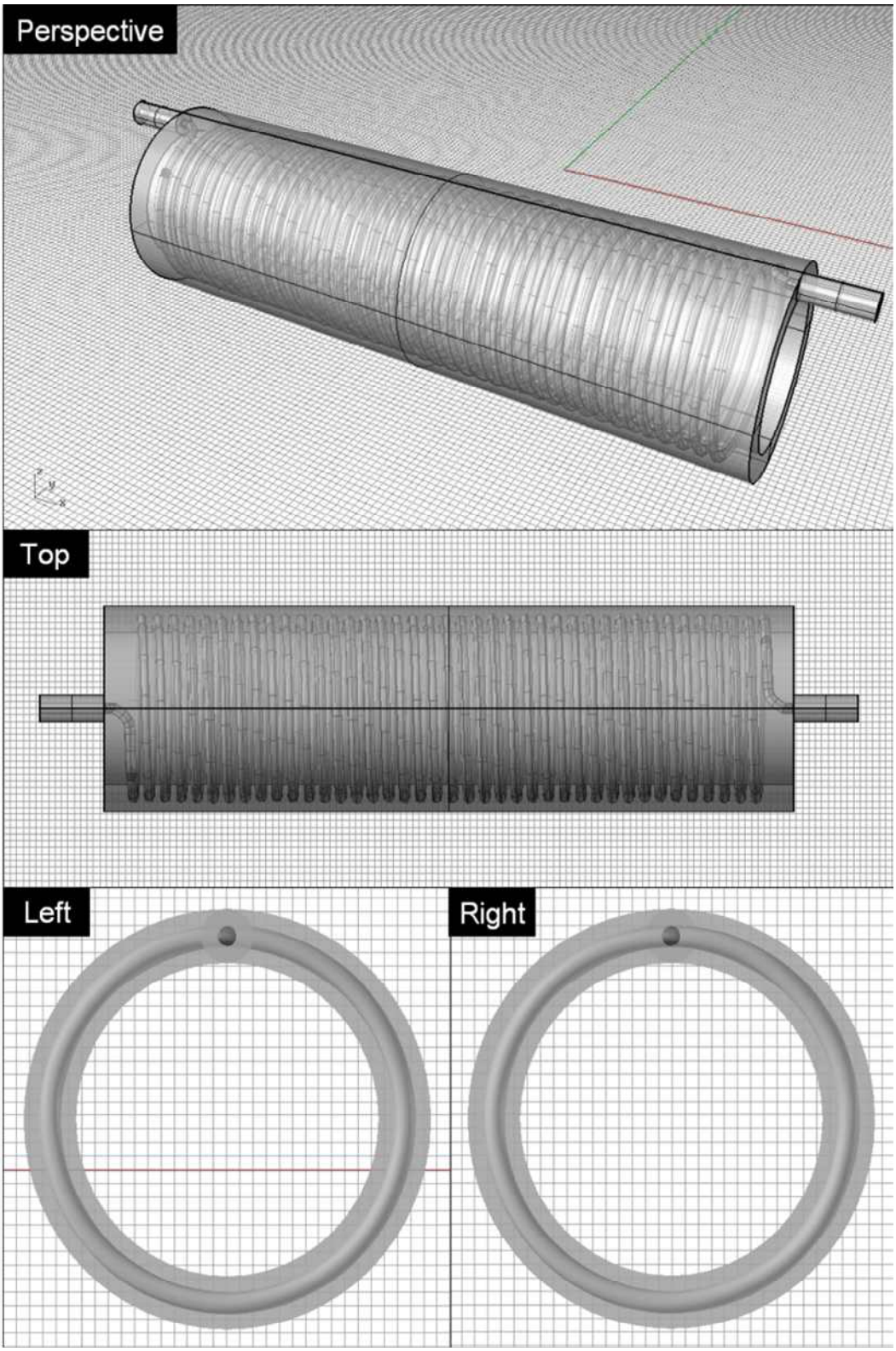

Fig. 5.1 Blueprint of helical-pipe splitter

5.1.2 Printing

Stereolithography (SLA) 3D printer, Form 1+ (Formlabs), was used for printing a helical-pipe splitter since the transparency of photopolymer resin could allow us to observe the passage inside the splitter. SLA is a printing technology that directs a laser beam across a tank of liquid resin to solidify layers. Once a layer is solidified, the build platform moves upward, and the next layer is solidified. The building volume is 125 × 125 × 165 mm, and the laser spot size is 155 ㎛.

Fig. 5.2. shows the printing process of the splitter. The layer thickness was 50 ㎛. A 405-nm wavelength violet laser beam with 120 mW was used.

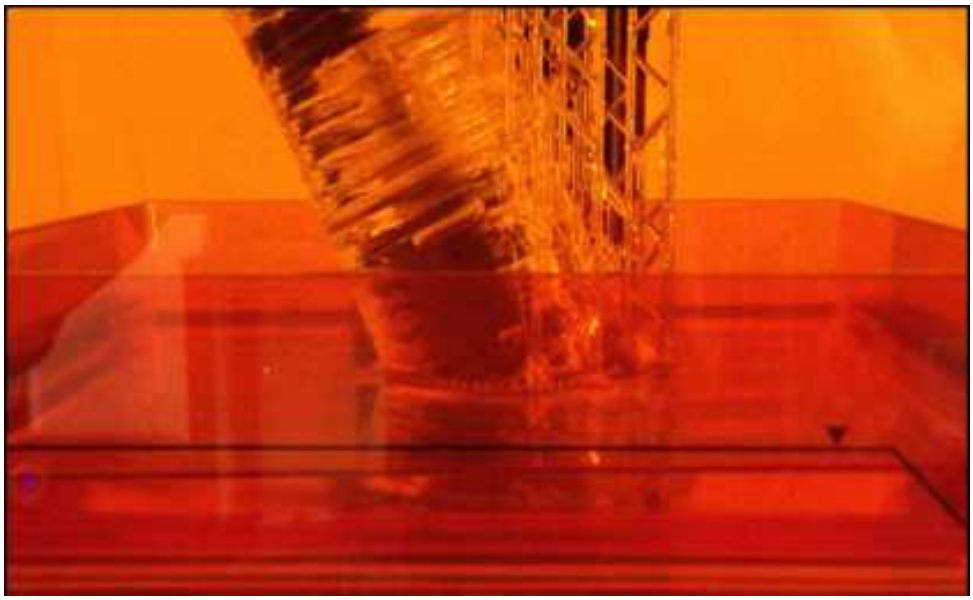

Fig. 5.2 Printing process of helical-pipe splitter

The material used for the printing process was clear photopolymer resin (Formlabs). The solidified resin had a tensile strength of 61.5 MPa at the yield point, which is equal to 615

atm, and this is sufficiently strong to resist the high pressure in pipe flow. The properties of the material are described in Table 5.1. The data represents post-cured properties obtained after exposing the material to 15 J/㎠ of UV light. Fig. 5.3 shows the 3D printer and the material used for the printing process.

Table 5.1 Properties of material

Property	Value
Tensile strength at yield	61.5 MPa
Young's modulus	2.7 GPa
Elongation at failure	5 %
Flexural modulus	2.38 GPa
Heat deflection temperature at 66 psi	78 ℃
Heat deflection temperature at 200 psi	60 ℃
5% Wt loss temperature	274 ℃

Fig. 5.3 3D printer and material used for printing

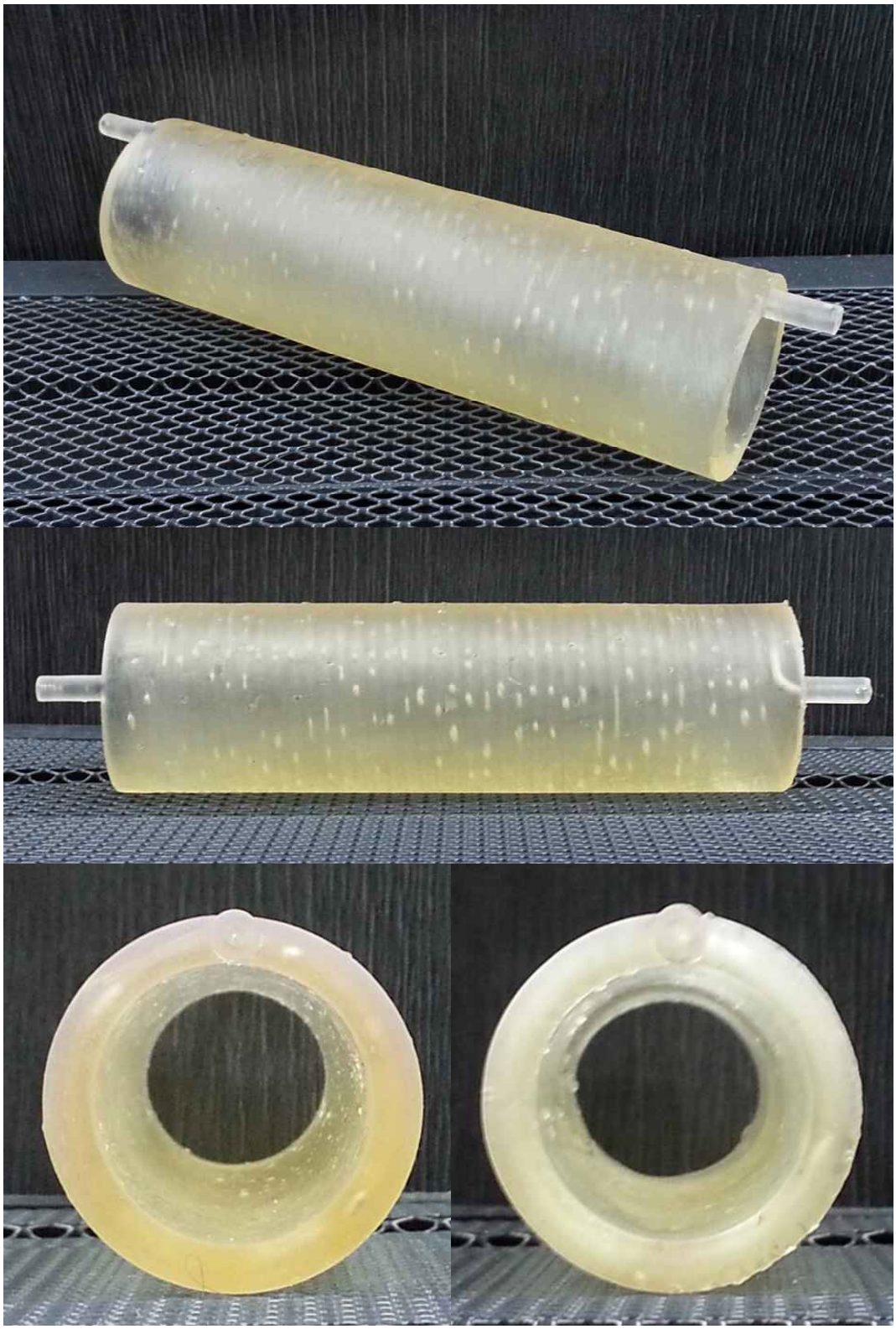

Fig. 5.4 3D-printed helical-pipe splitter

Fig. 5.4 shows the printed helical-pipe splitter, and Table 5.2 describes the specifications of the 3D-printed helical-pipe splitter.

Table 5.2 Properties of 3D-printed helical-pipe splitter

Properties	Value
Length(m)	2.5
Diameter(mm)	2
Roughness($s/m^{1/3}$)	N/A
Helical Radius(mm)	10
Pitch(mm)	3
Volume(㎤)	35.2
Mass(g)	37.5

5.2 DO concentration experiment on 3D-printed helical-pipe splitter

5.2.1 Experiment materials and methods

The same experimental set-up that was used in the experiment for the straight-pipe splitter described in Chapter 3.3 was used. The splitter was changed from a hose-coiled splitter to a 3D-printed splitter. Four 3D-printed helical-pipe

splitters, shown in Fig. 5.4, were connected in series such that the length of the splitter was 10 m.

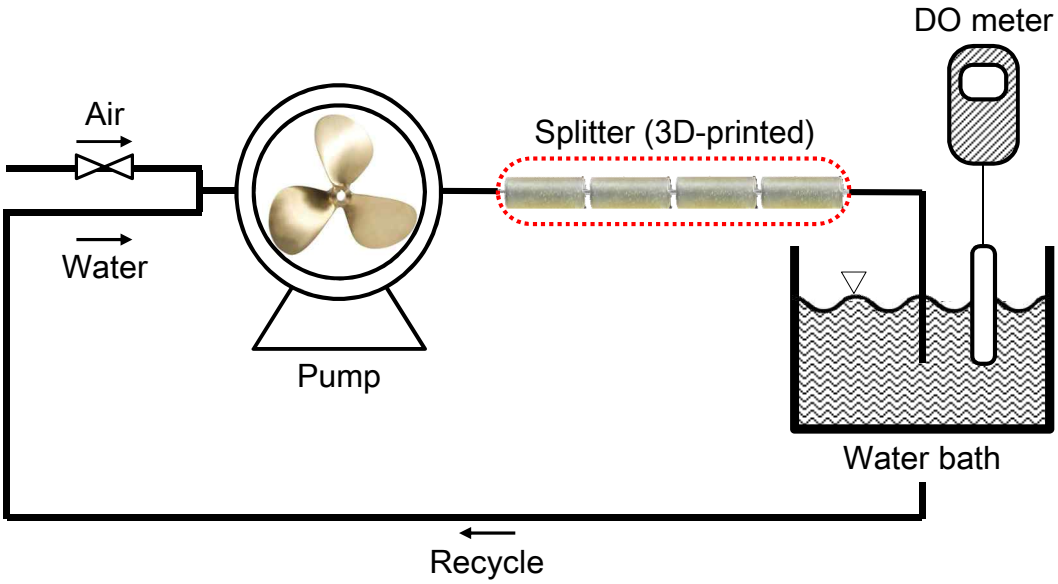

Fig. 5.5 Schematic diagram of DO measurement experiment of 3D-printed helical-pipe splitter

Fig. 5.5 shows the schematic diagram of the experiment. Tap water and air are drawn into the generator by the pump, and the mixture is split by the shear force of the pipe splitter. The DO concentration was measured by a DO meter placed in the middle of a water bath for 60 min. The DO concentration was measured in 1-min interval for the first 10 min, and then in 5-min intervals for the remaining 50 min. The designated dashed line represents the place where the 3D-printed helical-pipe splitter is connected.

5.2.2 Experiment results

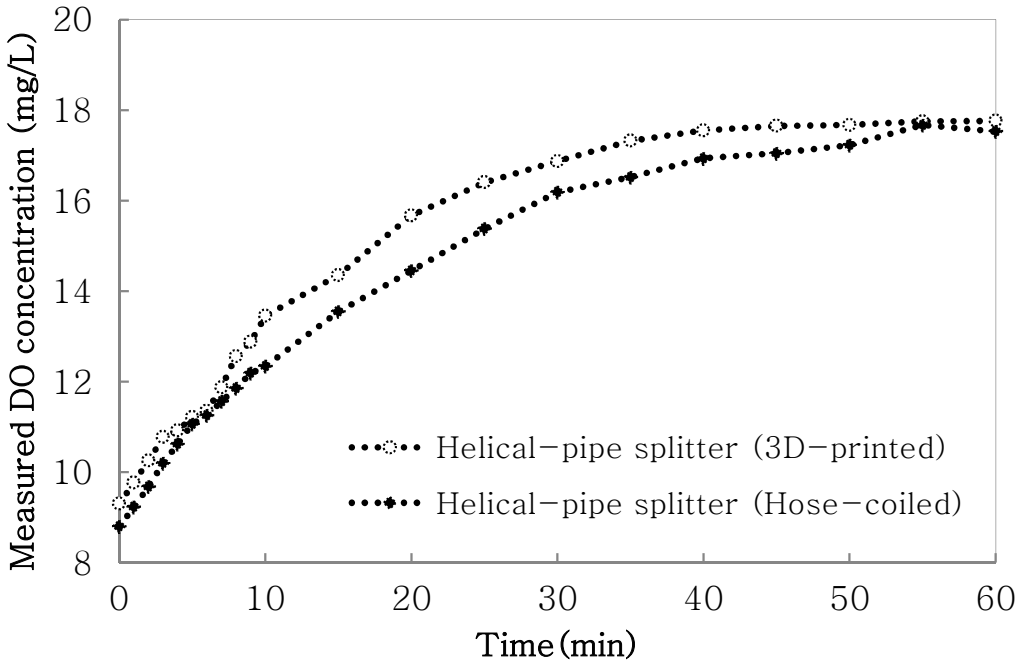

Fig. 5.6 DO concentration change for hose-coiled and 3D-printed helical-pipe splitters

Fig. 5.6 shows the change in DO concentration for the 3D-printed helical-pipe splitter, and the comparison with the results of the previous hose-coiled helical-pipe splitter. The two curves showed similar trends of increasing over time until a certain point and became constant after that point. The initial DO concentrations of the two curves were 8.80 mg/L and 9.30 mg/L, respectively. The final DO concentrations were 17.53 mg/L and 17.76 mg/L, respectively. During the experiment, the temperature of water was maintained between 16.7-19.6 ℃.

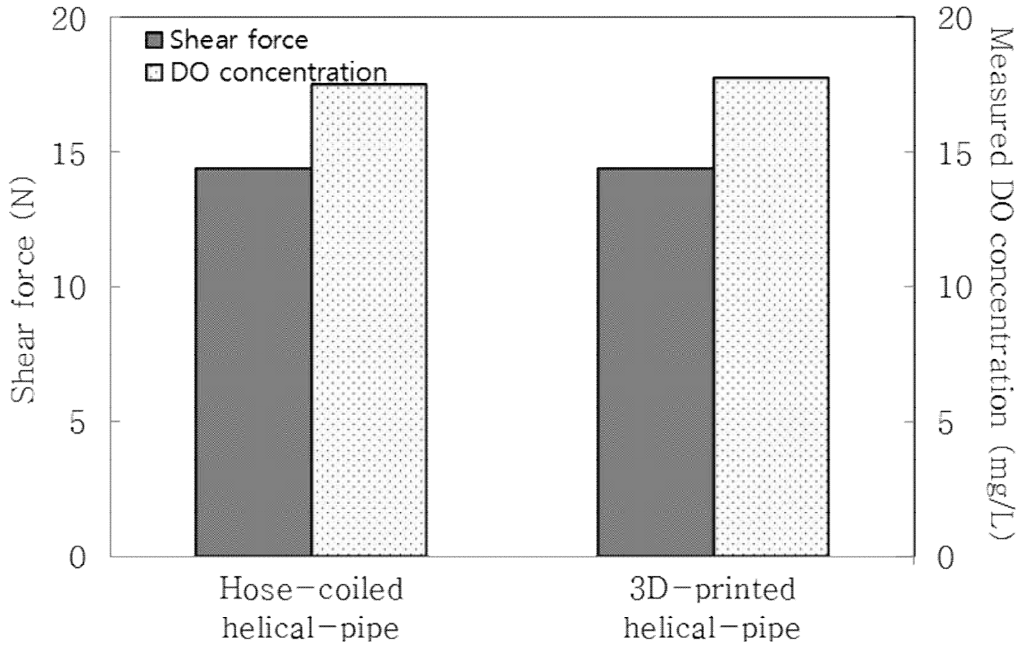

Fig. 5.7 Comparison of hose-coiled and 3D-printed helical-pipe splitters

Fig. 5.7 represents the shear force and DO concentration for the hose-coiled and 3D-printed helical-pipe splitters. It seems that there is no noticeable difference of the shear force and DO concentration between the hose-coiled and 3D-printed helical-pipe splitters. This is reasonable because, except the pitch, the specifications of both the splitters are almost identical, and the pitch is assumed to have little effect on both the shear force and DO concentration.

5.3 Reduction of the volume and mass

Table 5.3 represents the volume and mass of the hose-coiled helical-pipe splitter and 3D-printed helical-pipe splitter. Although the two pipes had the same length, diameter, and helical radius, the volume and mass of the hose-coiled helical-pipe splitter were 290.4 cm^3 and 280.0 g, respectively, while those of the 3D-printed helical-pipe splitter were 140.8 cm^3 and 150.0 g, respectively. In this case, the introduction of 3D printing reduced the volume and mass by 48.5% and 53.6%, respectively. It is mainly attributable to the reduction of the pitch from 6 mm to 3 mm in the 3D-printed helical-pipe splitter. These findings imply that the introduction of 3D printing can significantly reduce the volume and mass and increase the mobility of helical-pipe splitters.

Table 5.3 Comparison of volume and mass between hose-coiled and 3D-printed helical-pipe splitters

Properties	Hose-coiled helical-pipe splitter	3D printed helical-pipe splitter
Length(m)	10	10
Diameter(mm)	2	2
Radius(mm)	10	10
Pitch(mm)	6	3
Volume(cm^3)	290.4	140.8
Mass(g)	280.0	150.0

5.4 Further research

With regard to future research on the splitter of a bubble generator, more complex design factors could be considered. As shown on the left side in Fig. 5.8, an introduction of pipe-in-pipe splitter could be considered as a method of increasing the surface area of the splitter, which, in turn, will exert a higher shear force on the passing bubbles. Furthermore, as shown on the right side of Fig. 5.8, a vortex-generating surface could be considered as a method of generating fine bubbles. Such studies need precise designs of the inner structure, which will require sophisticated and elaborate fabrication by 3D printing. The efficiency of bubble generation could be increased by conducting further studies by considering the two factors mentioned above.

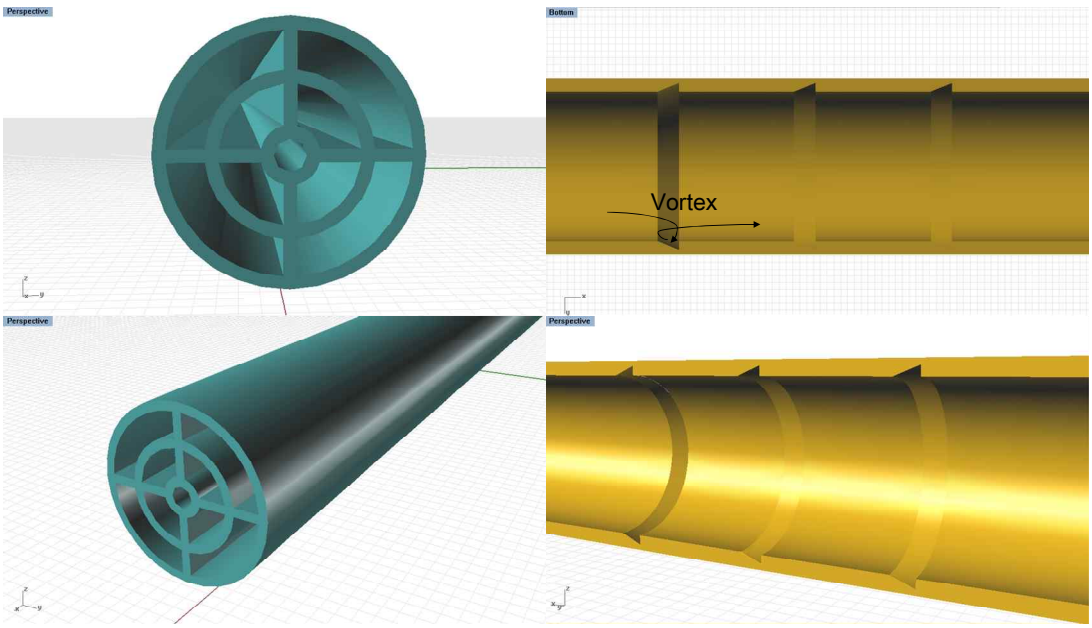

Fig. 5.8 Further research:
Pipe-in-pipe (left) and vortex-generating surface (right)

Chapter 6. Bubble Size Measurement

Image analysis is considered to be the most reliable method for measurement of bubble size. However, because of the diffraction limit of conventional lenses, it is impossible to resolve separate points less than 200 nm with an optical microscope. Moreover, if the sample bubble is in motion within a liquid medium, precise measurement is more difficult.

Table 6.1 Bubble size measurement methods

Bubble size measurement method	Size	Measurement time
Dynamic light scattering (DLS)	0.5–10 μm	5 min
Particle tracking analysis (PTA)	0.05–1 μm	≤ 1 min
Laser diffraction (LD)	0.01–1,000 μm	10 s
Resonance mass measurement (RMM)	0.12–1 μm	≤ 15 min
Electrical sensing zone method	0.05–1 μm	10 min
Ultrasound	0.1–1,000 μm	1 min
Optical particle counter	2–100 μm	30 s
Static image analysis	1–100 μm	N/A
Static multiple light scattering (SMLS)	0.01–100 μm	≤ 10 s

Therefore, several studies have been conducted for developing a precise and reasonable size measurement method for fine bubbles smaller than 100 μm. Table 6.1 lists the widely used bubble size measurement methods.

For reference, technical committee 281 of the International Standardization Organization (ISO/TC 281), established in 2013, works on standardization of fine bubble technology covering general principles including terminology, characterization, and applications of fine bubbles.

6.1 Ultrasound irradiation

Table 6.2 Color change by ultrasound irradiation (Kim, 2010)

	Distilled water	Nano bubble water
Before irradiation		
After irradiation		

Kim (2010) developed an indirect confirmation method that can determine the generation of fine bubbles by color change caused by ultrasound irradiation. According to his theory, nano bubbles less than 700 nm turns white upon ultrasound irradiation because nano bubbles coalesce to generate micro bubbles that appear white, and the micro bubbles quickly rise to the fore and disappear. On the contrary, there is no color change in distilled water upon irradiation. Table 6.2 shows the color change of nano bubbles water upon ultrasound irradiation (28 KHz).

6.1.1 Experiment materials and methods

The same experiment set-up described in Chapters 3 and 4 was used, except the water bath, which was replaced with an ultrasound irradiator (SH-2300, Shaehan sonic), as shown in Fig. 6.1. The frequency of sound was set as 28 KHz. Then, the same ultrasound was used to irradiate 10 different outflows that were generated under the same conditions as those in the previous 10 experiments conducted in Chapters 3 and 4.

Fig. 6.1 Ultrasound irradiator

6.1.2 Experiment results

Table 6.3 summarizes the results of the color change, using ultrasound irradiation. All cases, except experiment number 3, showed color change which means the generation of fine bubble. These results showed fair agreement with the predicted shear force and the measured DO concentration. However, it was difficult to compare the extent of color change among each splitter.

Table 6.3 Summary of color change by ultrasound irradiation

No.	L (m)	D (㎜)	f ($s/m^{1/3}$)	R (㎜)	P (㎜)	Shear force (N)	DO (mg/L)	Color change
1	5	2	0.010	–	–	0.80	13.81	○
2	10	2	0.010	–	–	5.04	15.77	○
3	5	4	0.010	–	–	0.56	9.71	×
4	5	2	0.012	–	–	1.26	15.23	○
5	10	2	0.010	100	6	11.03	16.04	○
6	5	2	0.010	100	6	5.51	14.17	○
7	10	4	0.010	100	6	3.60	11.05	○
8	10	2	0.012	100	6	11.90	16.71	○
9	10	2	0.010	10	6	14.40	17.53	○
10	10	2	0.010	100	12	11.04	15.92	○

6.2 Empirical relationship between bubble size and measured DO concentration

Kim (2014) developed an empirical relationship between bubble size and DO concentration measured using a DO meter (ProODO, YSI). Fig. 6.2 illustrates the principle of measuring DO concentration with an optical DO meter. Oxygen is constantly moving through a diffusion layer inside the probe, and affects the luminescence of the sensing layer. By comparing the lifetime of luminescence measured by the sensor against the reference, the DO concentration is obtained. The lifetime of luminescence in the sensing layer is inversely proportional to the amount of oxygen passing through the layer (YSI, n.d.).

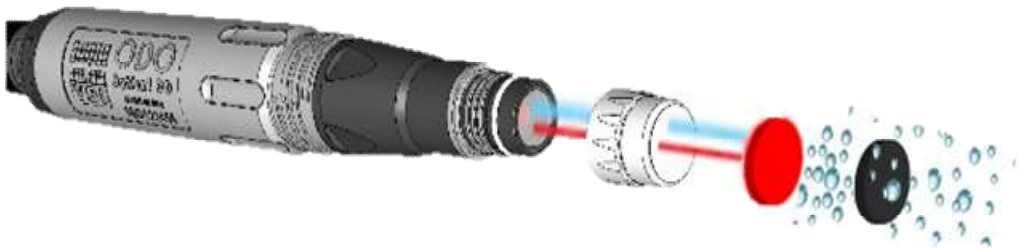

Fig. 6.2 Principle of optical DO meter

According to his theory, there is a marginal size (n) of bubbles that can pass through the sensing layer and can lead to an overestimation of DO concentration compared to that of Winkler titration.

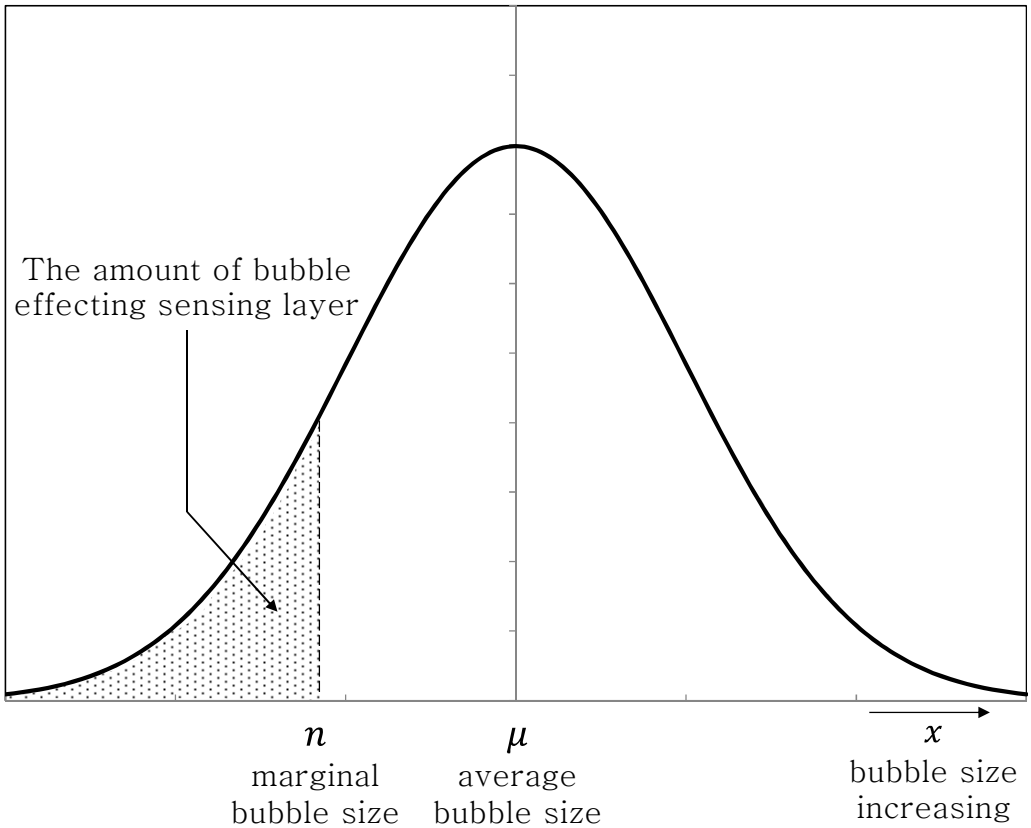

Fig. 6.3 The amount of bubble affecting sensing layer

Based on earlier findings that bubble size distribution follows normal distribution (Liao and Lucas, 2009), an empirical relationship, as shown in Eq. (6.1), was derived from the relationship between the calculated area under the normal distribution curve, where the bubble size (x) is less than the marginal bubble size (n), and the experiment results of DO concentration, as shown in Fig. 6.3.

$$y = \frac{1}{2} a \left(1 + erf \frac{b - x}{c\sqrt{2}}\right) + d \qquad \text{Eq. (6.1)}$$

In the equation above, y denotes the DO concentration, x denotes the average bubble size and a, b, c, and d are constants having values of 7248.48, -7.69, 3.16, and 10.31, respectively.

Fig. 6.4 shows the relationship between the DO concentration measured by the optical DO meter and the bubble size.

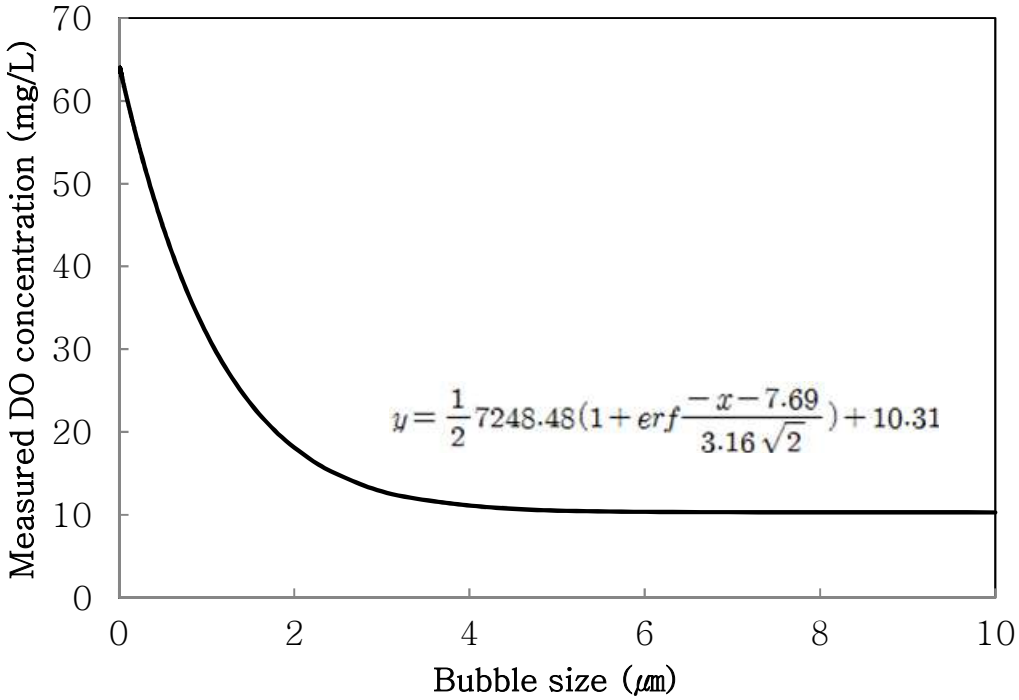

Fig. 6.4 Empirical relationship between bubble size and measured DO concentration (Kim, 2014)

Table 6.4 represents the average bubble sizes obtained by the application of this empirical equation by Kim (2014) to the previous 10 experiment results described in Chapters 3 and 4. The results showed reasonably good agreement with the

predicted shear force and the measured DO concentration. However, it was difficult to quantify the extent of color change with this method.

Table 6.4 Estimated bubble size by empirical equation with DO concentration

No.	L (m)	D (mm)	f ($s/m^{1/3}$)	R (mm)	P (mm)	Shear force (N)	DO (mg/L)	Avg. bubble size (μm)
1	5	2	0.010	–	–	0.80	13.81	2.74
2	10	2	0.010	–	–	5.04	15.77	2.34
3	5	4	0.010	–	–	0.56	9.71	N/A
4	5	2	0.012	–	–	1.26	15.23	2.43
5	10	2	0.010	100	6	11.03	16.04	2.29
6	5	2	0.010	100	6	5.51	14.17	2.65
7	10	4	0.010	100	6	3.60	11.05	4.04
8	10	2	0.012	100	6	11.90	16.71	2.19
9	10	2	0.010	10	6	14.40	17.53	2.08
10	10	2	0.010	100	12	11.04	15.92	2.31

6.3 Static image analysis with confocal microscopy

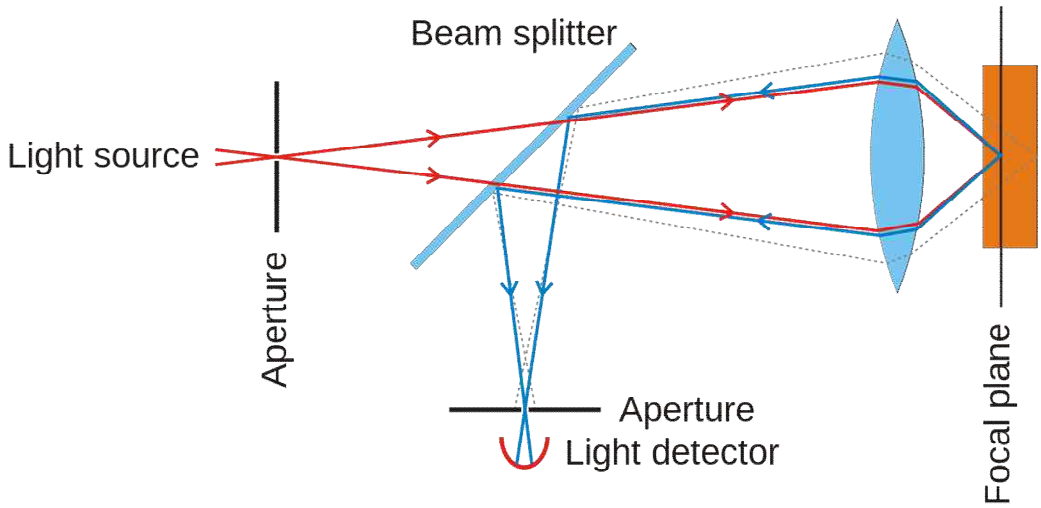

Fig. 6.5 Principle of confocal microscopy (Wikipedia, n.d.)

Confocal microscopy is a widely used optical imaging technique in the field of biology, physics, and material science that can provide images with a higher resolution and contrast by eliminating out-of-focus light by placing a pinhole on the path from a light source through lens, sample, and light detector. If sequential images were obtained by moving a confocal plane in the direction of the z-axis, three-dimensional structures can be constructed. Because confocal microscopy enables non-destructive and non-contact measurement, it is highly suitable for imaging a bubble in a liquid medium. Fig. 6.5 shows the principles of confocal microscopy.

6.3.1 Experiment materials and methods

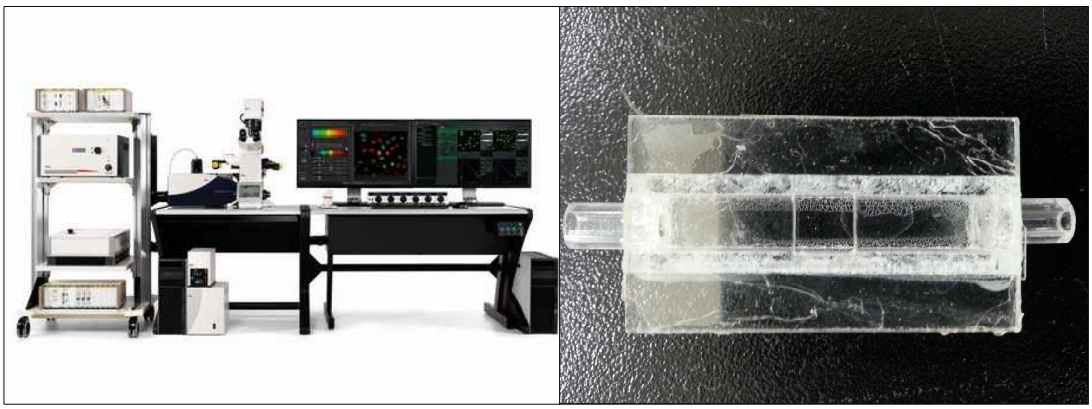

Fig. 6.6 Confocal microscope (left) and measurement cell (right)

Fig. 6.6 shows a confocal microscope (TCS SP8, Leica) and a measurement cell (1 × 1 × 5 cm). The outflow water of the bubble generator in experiment number 9 was sampled and taken into the confocal plane. Fig. 6.7 shows the schematic diagram of the measurement.

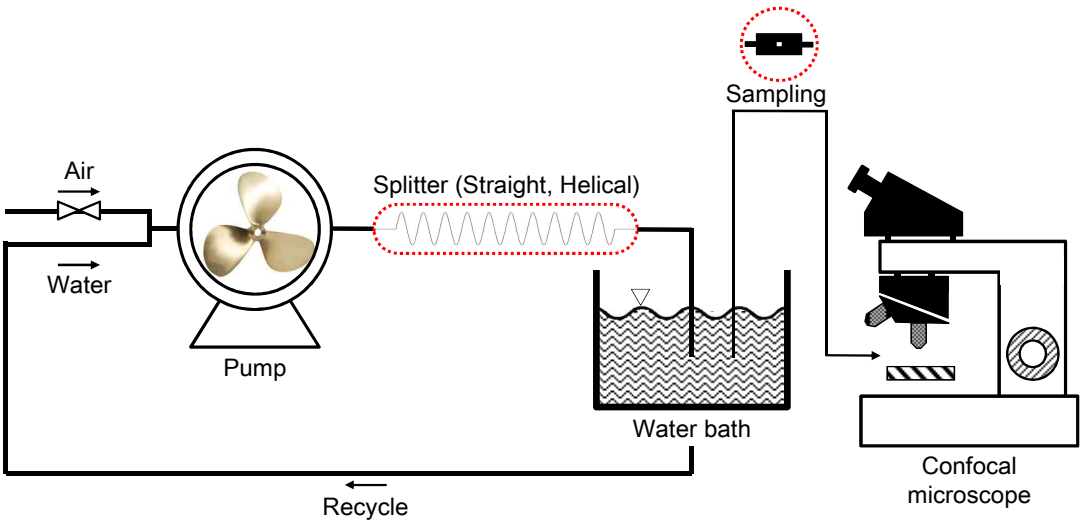

Fig. 6.7 Schematic diagram of bubble measurement using confocal microscope

Due to a vague boundary between water and bubble, the photos taken by the confocal microscope need an edge detection process. The points at which image brightness changes sharply were presumed as edges. The microscope's software (LAS AF Lite, Leica) and a graphic editor (Photoshop CC, Adobe) were used for the process.

The bubble sizes were obtained through the following steps: ① removing hue and saturation, ② edge detection, ③ enlarging and pixelation, and ④ counting and calculation.

Fig. 6.8 shows the original image obtained by the confocal microscope. Fig. 6.9 shows the image obtained after hue and saturation removal. Fig. 6.10 shows the processed image with edge detection. Fig. 6.11 shows the enlarged and pixelated image. Fig. 6.12 shows the counting.

In the example below, each pixel (0.090 × 0.090 μm) has an area of $8.26 \times 10^{-3}\,\mu m^2$, and the number of pixel is 114. The calculated diameter of this bubble is 533 nm, which represents the bubble size.

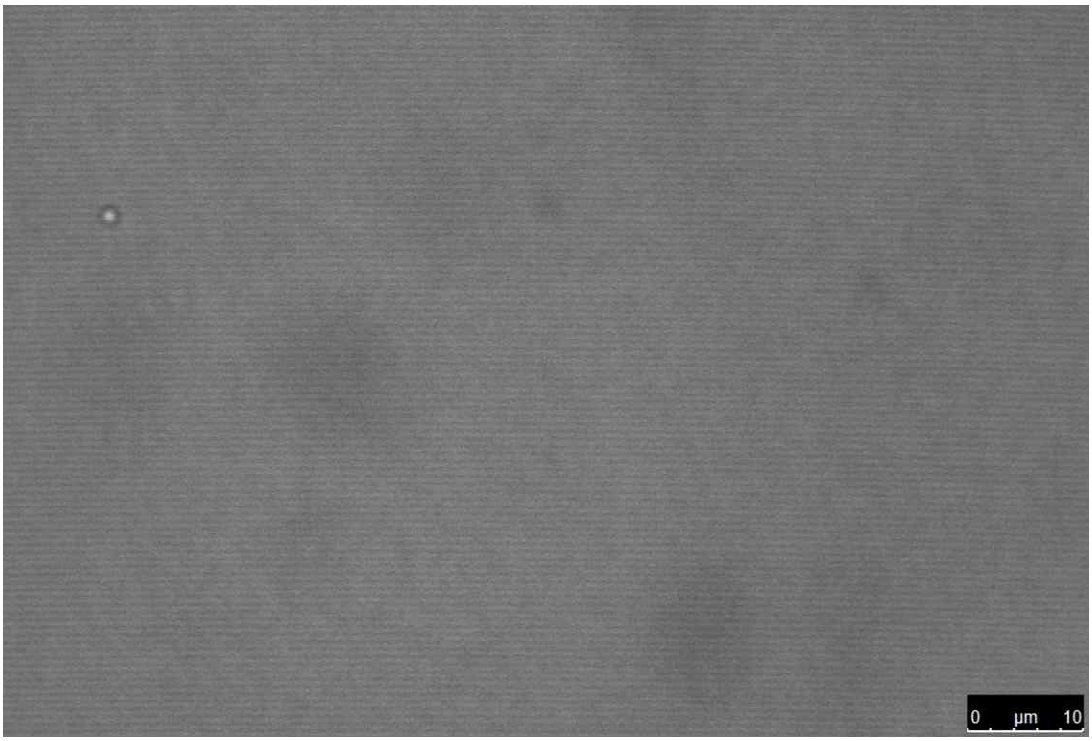

Fig. 6.8 Original image

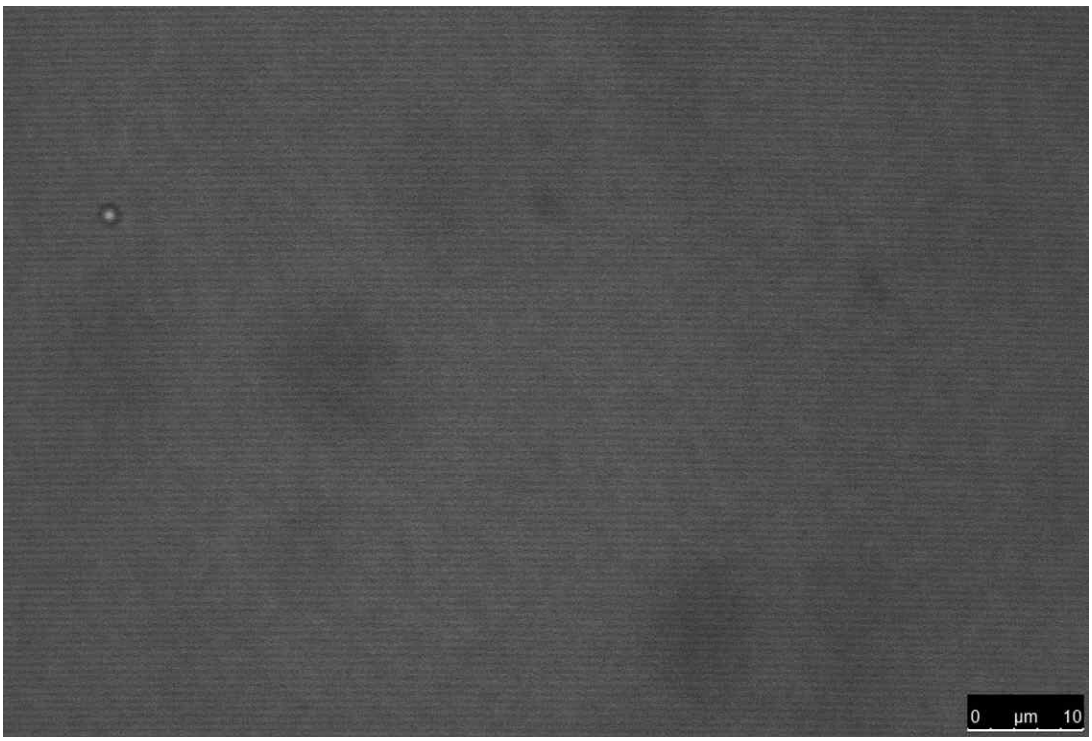

Fig. 6.9 Processed image with hue and saturation removal

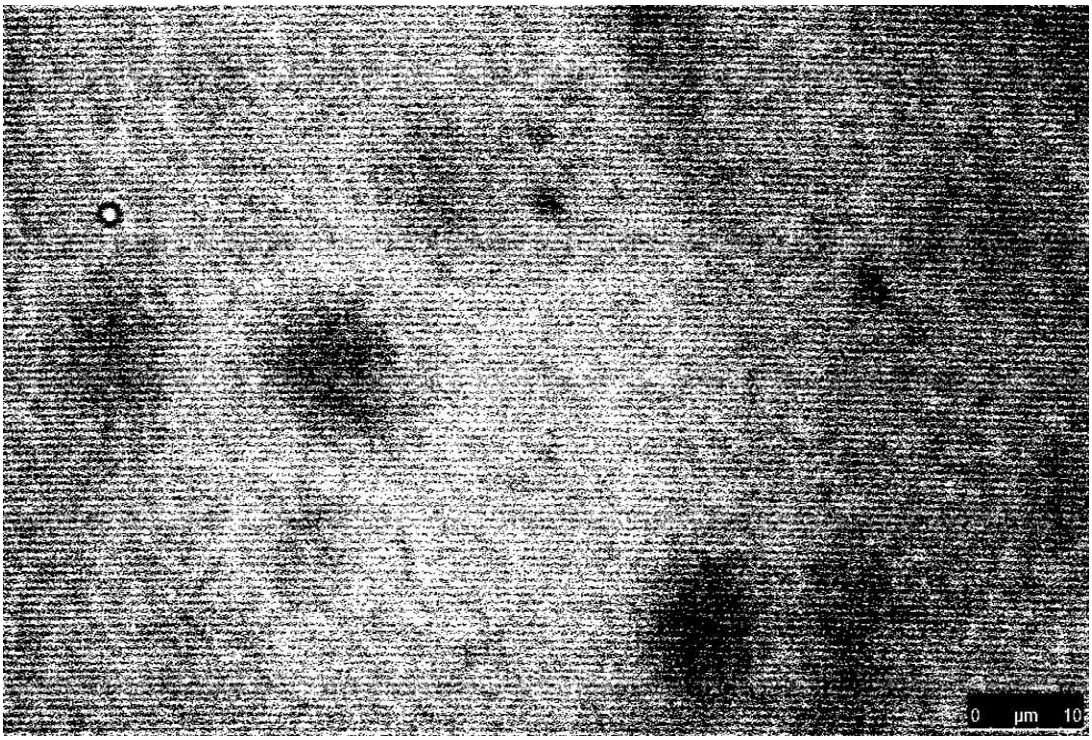

Fig. 6.10 Processed image with edge detection

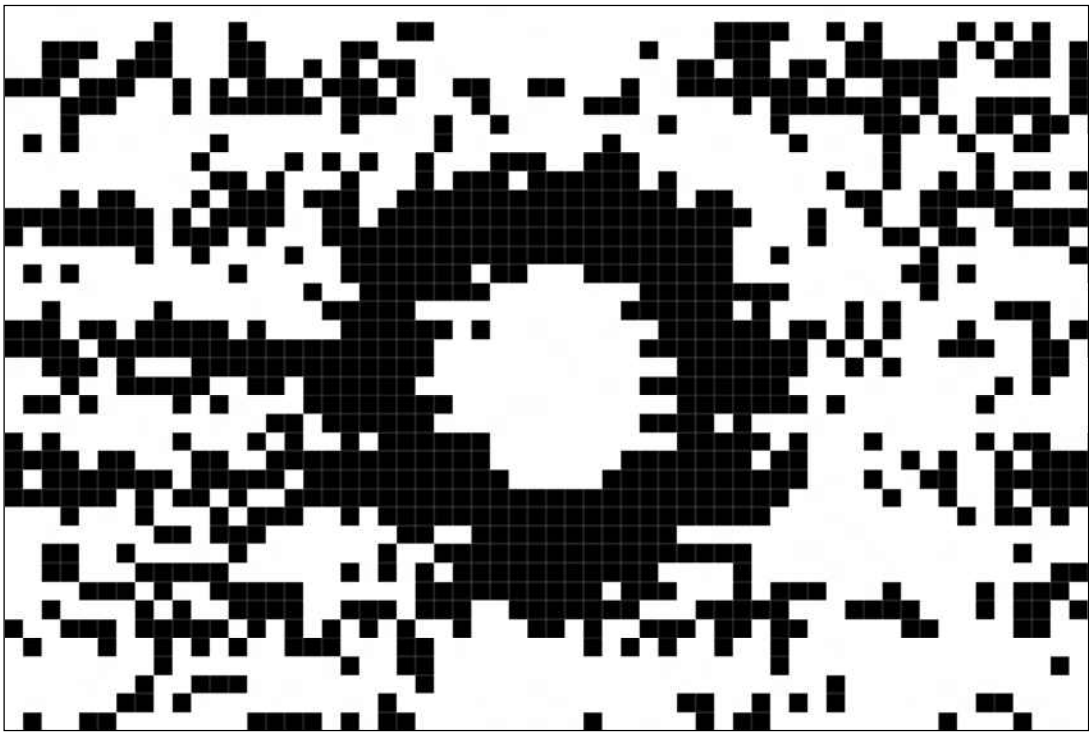

Fig. 6.11 Processed image with enlarging and pixelation

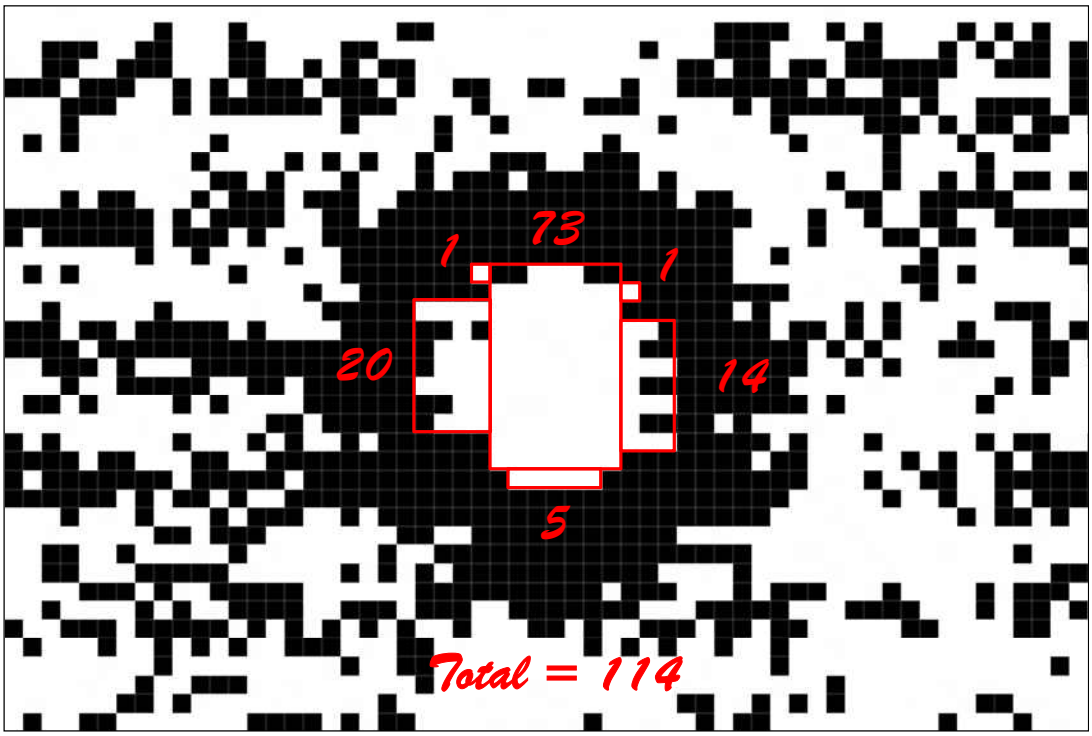

Fig. 6.12 Counting pixels

6.3.2 Experiment results

Table 6.5 summarizes the specifications of bubbles generated from the straight-pipe and helical-pipe splitters, obtained using the static image analysis with confocal microscopy.

The average bubble size, standard deviation, smallest and largest bubble size of the straight-pipe splitter were 0.683 μm, 0.506 μm, 0.324 μm, and 1.664 μm, respectively.

The average bubble size, standard deviation, smallest and largest bubble size of the helical-pipe splitter were 0.433 μm, 0.378 μm, 0.103 μm, and 1.361 μm, respectively.

Table 6.5 Bubble size measurement by confocal microscopy

Straight-pipe (No. 2)		Helical-pipe (No. 9)	
No.	Bubble size (μm)	No.	Bubble size (μm)
1	0.324	1	0.103
2	0.370	2	0.115
3	0.410	3	0.154
4	0.431	4	0.162
5	0.435	5	0.316
6	0.508	6	0.462
7	0.533	7	0.526
8	0.552	8	0.548
9	1.605	9	0.589
10	1.664	10	1.361
Average bubble size (μm)	0.683	Average bubble size (μm)	0.433
Standard deviation (μm)	0.506	Standard deviation (μm)	0.378

Even though the number of samples was inadequate, the results showed good agreement with the previous conclusion in Chapter 4.6 that helical pipes are more effective in splitting than straight pipes.

For reference, while confocal microscopy is advantageous for measuring individual bubble size, a lot of effort and time is required for focusing and image processing. Therefore, it is not an effective method of analyzing the size distribution of a large amount of bubbles.

Chapter 7. Conclusion

It was originally assumed that a helical pipe would be more effective in generating fine bubbles (or micro/nano bubbles) than a straight pipe as a splitter of a splitting-type fine bubble generator.

The findings showed good agreement with the hypothesis. With the introduction of a helical radius, the shear force exerted on pipe flow increased, the measured DO concentration increased, and the bubble size decreased. One possible explanation is that torsion introduced by the helical radius forces the flow to keep moving in a straight direction and increases the wall shear stress exerted on pipe flow. The results obtained showed good agreement with those of Gammack and Hydon (2001).

This study aimed to define the relationship between the efficiency of bubble generation and design factors at a particular flow-rate, temperature, air-water composition ratio, and type of gas. It is possible to obtain different results by using different experiment set-ups and performing the experiments under different conditions.

The approach outlined in this study should be replicated under different conditions by considering more various design factors in order to construct advanced correlations. Based on the findings that a helical pipe offers distinct advantages over a conventional straight pipe, the introduction of a helical pipe as a splitter would be beneficial to increase the efficiency of a splitting-type bubble generator.

List of References

Agarwal, A., Ng, W. J., & Liu, Y. (2011). Principle and applications of microbubble and nanobubble technology for water treatment. Chemosphere, 84(9), 1175-1180.

Berger, S. A., Talbot, L., & Yao, L. S. (1983). Flow in curved pipes. Annual review of fluid mechanics, 15(1), 461-512.

Berman, B. (2012). 3-D printing: The new industrial revolution. Business horizons, 55(2), 155-162.

Cassaignau, A. (2015, April 30). Understanding our 60 ㎛ layer thickness printing setting. Sculpteo. Retrieved from http://www.sculpteo.com/blog/2015/04/30/60%C2%B5m-layer-thickness-3d-printing/

Chua, C. K., Leong, K. F., & Lim, C. S. (2010). Rapid Prototyping: Principles and Applications 3rd. World Scientific.

Confocal microscopy. (n.d.). Retrieved January 27, 2016 from https://en.wikipedia.org/wiki/Confocal_microscopy

Dockko, S., & Han, M. Y. (2004). Fundamental characteristics of bubbles and ramifications for the flotation process. Water science and technology: a journal of the International Association on Water Pollution Research, 50(12), 207.

Edzwald, J. K. (1995). Principles and applications of dissolved air flotation. Water Science and Technology, 31(3), 1-23.

Gammack, D., & Hydon, P. E. (2001). Flow in pipes with non-uniform curvature and torsion. Journal of fluid mechanics, 433, 357-382.

Germano, M. (1982). On the effect of torsion on a helical pipe flow. Journal of Fluid Mechanics, 125, 1-8.

Grindley, J. H., & Gibson, A. H. (1908). On the Frictional Resistances to the Flow of Air through a Pipe. Proceedings of the Royal Society of London. Series A, Containing Papers of a Mathematical and Physical Character, 80(536), 114-139.

ISO/TC 281 Fine Bubble Technology. (2013). Retrieved January 27, 2016 from http://www.iso.org/iso/iso_technical_committee?commid=4856666

Kao, H. C. (1987). Torsion effect on fully developed flow in a helical pipe. Journal of Fluid Mechanics, 184, 335-356.

Kim, H. J. (2014). A study on sub-micron bubble generator and its application (Doctoral dissertation, PHD thesis, Seoul National University, Seoul).

Kim, T. I. (2010). Analysis of bubble potential energy and its application to disinfection and oil washing (Doctoral dissertation, PHD thesis, Seoul National University, Seoul).

Kiuru, H., & Vahala, R. (2001). Dissolved air flotation in water and waste water treatment. In International Conference on DAF in Water and Waste Water Treatment 2000: Helsinki, Finland). IWA Publishing.

Melchels, F. P. (2012). Celebrating three decades of stereolithography. Virtual and Physical Prototyping, 7(3), 173-175.

Motarjemi, M., & Jameson, G. J. (1978). Mass transfer from very small bubbles—the optimum bubble size for aeration. Chemical Engineering Science, 33(11), 1415-1423.

Munson, B. R., Young, D. F., Okiishi, T. H., & Huebsch, W. W. (2009). *Fundamentals of fluid mechanics 6th edition*. New York.

ProODO specifications. (n.d.). Retrieved January 27, 2016 from https://www.ysi.com/File%20Library/Documents/Specification%20Sheets/W3-05-ProODO.pdf

Rifkin, J. (2011). The third industrial revolution: how lateral power is transforming energy, the economy, and the world. Macmillan.

Scardina, R. P. (2000). Water Treatment: Fundamentals and Practical Implications of Bubble Formation.

Three-dimensional printing. (n.d.). Retrieved January 27, 2016 from https://en.wikipedia.org/wiki/3D_printing

Vaezi, M., & Chua, C. K. (2011). Effects of layer thickness and binder saturation level parameters on 3D printing process. The International Journal of Advanced Manufacturing Technology, 53(1-4), 275-284.

Wang, L. K., Hung, Y. T., Lo, H. H., & Yapijakis, C. (Eds.). (2004). Handbook of industrial and hazardous wastes treatment. CRC Press.

Wang, C. Y. (1981). On the low-Reynolds-number flow in a helical pipe. Journal of Fluid Mechanics, 108, 185-194.

Yamamoto, K., Yanase, S., & Yoshida, T. (1994). Torsion effect on the flow in a helical pipe. Fluid Dynamics Research, 14(5), 259.

국 문 초 록

미세기포를 발생시키는 원리 중 하나는 스플리터라고 불리는 길고 가는 관로의 벽면이 유체에 가하는 전단력을 이용해 관로를 따라 흐르는 유체 내의 기포를 더욱 작은 기포로 쪼개는 것이다.

본 연구는 관수로의 전단력을 이용한 미세기포 발생장치에서 스플리터의 기하학적 구조가 직선형에서 나선형으로 변화함에 따라 나타나는 발생기포의 크기변화를 분석하는 것을 목적으로 하였다.

이를 위해 10 개의 서로 다른 설계조건을 가진 스플리터에 대해 전산유체동역학(CFD)을 이용한 전단력 모델링, 용존산소(DO) 농도 측정 실험, 공초점 현미경을 이용한 화상분석을 수행하였다.

수행결과, 나선형 기하구조의 도입에 따라 유체에 가해지는 전단력과 DO 농도는 증가하고, 기포크기는 감소하는 것으로 나타났다. 이러한 결과는 나선형 스플리터의 도입이 발생기포의 크기를 줄여 미세기포발생장치의 효율을 높일 수 있음을 의미한다.

주요어: 나선형 관수로, 미세기포, 스플리터, 전단력, 용존산소

학 번: 2014-20552